ABSTRACT

Title of Thesis: EXPERIMENTAL INVESTIGATION INTO THE HEAT TRANSFER MECHANISM OF OSCILLATING HEAT PIPES USING TEMPERATURE SENSITIVE PAINTS

Matthew Francom, M.S., 2020

Thesis Directed By: Professor Jungho Kim, Department of Mechanical Engineering

Oscillating heat pipes (OHPs) represent a promising passive mechanism for the removal or spreading of heat. While simple to construct, the fluid and thermodynamics of these devices are still poorly understood. There is debate over whether the primary heat transfer mechanism is due to sensible heating of the liquid phase or due to latent heat transfer through phase change. To provide experimental data answering this question, an experimental apparatus was constructed to provide local temperature and heat transfer data across the face of an OHP during operation. This experiment utilized temperature sensitive paint alongside visual recording of the fluid motion in order to determine the relative latent and sensible contribution to the overall heat transfer. The OHP was tested with input powers ranging from 2.6 W to 10.1 W. It found that latent heat transfer was dominant, representing between 65% and 85% of the total heat transferred in all cases.

EXPERIMENTAL INVESTIGATION INTO THE HEAT TRANSFER MECHANISM OF OSCILLATING HEAT PIPES USING TEMPERATURE SENSITIVE PAINTS

by

Matthew Francom

Thesis submitted to the Faculty of the Graduate School of the
University of Maryland, College Park, in partial fulfillment
of the requirements for the degree of

Masters of Science

2020

Advisory Committee:
Professor Jungho Kim, Chair
Professor Reinhardt Radermacher
Professor Bao Yang

Acknowledgements

I would like to thank my advisor, Dr. Jungho Kim, for his assistance and advice throughout this project. I would further like to thank the members of the Phase Change Heat Transfer Lab, particularly Caleb Hammer and Cathleen Needham, for their advice and input. Their advice on the setup of the temperature sensitive paint used here, and on the setup and use of the cameras used for this project, were especially valuable. Finally, I would like to thank Dr. Eric Silk for his input on fluid mechanics and heat transfer mechanisms as related to heat pipes.

Table of Contents

Acknowledgements ii

Table of Contents iii

List of Figures v

List of Tables vii

1. Introduction 1

1.1. OHP Principle of Operation and Important Parameters 3

1.1.1. Fluid Properties 3

1.1.2. Effect of Geometry and Number of Turns 5

1.1.3. Fill Ratio 7

1.1.4. Other Considerations 7

1.2. Flow Regimes and Startup 9

1.3. Heat Transfer Mechanism 11

2. Experimental Overview 12

2.1. Experimental Theory and Setup 12

2.1.1. TSP Production, Application, and Calibration 15

2.1.2. TSP Response Time 19

2.1.3. Heat Pipe Geometry 20

2.1.4. Working Fluid 21

2.1.5. Filling Procedure 22

2.2. Adhesive Thermal Conductivity Measurement 24

2.3. Heat Transfer Uncertainty Analysis 26

2.4. Experimental Procedure 30

3. Data Conversion and Post-Processing 31

3.1. Image Processing 31

3.2. Bias Adjustment 31

3.3. Additional Heat Transfer Mechanisms 33

4. Performance and General Observations 36

5. Analysis of Heat Transfer Mechanism 39

5.1. Latent Heat Transfer Verification 40

5.2. Latent vs Sensible Selection 44

5.3. Results 47

6. Conclusion and Future Work 52

6.1. Conclusion 52

6.2. Suggested Changes to Design and Future Work 52

7. References 55

List of Figures

Figure 1: Schematic of a closed loop OHP [13]. 2

Figure 2: Heat pipe cross section and camera configuration (not to scale) 13

Figure 3: Visual (left) and TSP (right) images. Crosses used for coordination may be seen at left and at top right. Visual image is flipped left to right in order to coordinate locations. 15

Figure 4: Fit function for five representative pixels 17

Figure 5: Heat Pipe within heated enclosure. 18

Figure 6: Heat pipe channel geometry. All measurements are in mm. 21

Figure 7: Comparison of saturation pressure gradient with temperature for several fluids 22

Figure 8: Plumbing schematic for heat pipe fill..... 23

Figure 9: Thermal conductivity measurement schematic 25

Figure 10: Thermocouple calibration..... 25

Figure 11: Histogram of temperatures predicted by intensity-temperature fit for one pixel for 1000 images taken at 22.6°C and 42.2°C. 27

Figure 12: Sample sapphire temperature interpolation (right). Temperature image used for interpolation shown at left with dots (used for interpolation) highlighted in red. 31

Figure 13: Areas used for bias measurement, highlighted in red at left. An example of the heat flux used for bias measurement is shown at right. 32

Figure 14: Bias values used for each video, plotted again power applied to heat pipe. ... 33

Figure 15: Percentage of applied heat transferred through the sapphire. 35

Figure 16: Heat pipe thermal resistance variation with applied power. 38

Figure 17: Comparison of visual data (left), temperature data (right), and calculated heat flux (center). Heat transfer is reaches its largest magnitude along the vapor bubbles. Note the dryout of the bubble in the center channel shown here. 39
Figure 18: Calculated mass loss alongside polynomial fit used to determine its derivative. The values shown here correspond to the 5.13 W case shown in Figure 19. 43
Figure 19: TSP and visually estimated heat transfer for two vapor slugs within the heat pipe condenser. 43
Figure 20: Estimated relative error in latent heat transfer assumption. 44
Figure 21: Points used for sensible/latent heat transfer comparison. Visual data shown at left, with heat flux data at right. 45
Figure 22: Example phase selection showing points flagged for verification. The data mean, used to distinguish the phases, is shown by a dashed line. 47
Figure 23: Sensible and latent contributions to the overall heat flux for two different videos. Two traces are shown – the top (positive) from the evaporator and the bottom from the condenser. 48
Figure 24: Relative contribution of sensible and latent heat transfer to overall heat transfer. Positions listed relative to the lowermost edge of heat pipe channels. 49
Figure 25: Latent heat transfer contribution for all data sets in which the heat pipe was operational 49
Figure 26: Identified locations of vapor and liquid slugs within the heat pipe. Red is used to indicate liquid while blue indicates vapor. 50
Figure 27: Summary of calculated latent contribution. 51

List of Tables

Table 1: Calibration Temperatures 19

Table 2: Room temperature thermodynamic properties of commonly used working fluids 22

Table 3: Standard deviation in predicted temperature at each calibration point..... 28

1. Introduction

The rise of semiconductor based electronics has led to an increased demand for compact, passive devices able to effectively remove concentrated sources of heat. Oscillating heat pipes (OHPs), alternately called pulsating heat pipes (PHPs), offer a promising thermal solution for such problems. These devices are mechanically simple and easy to manufacture, and have experimentally demonstrated effective thermal conductivities in excess of two orders of magnitude above that of copper [1]–[3]. They have been tested at temperatures down to 17 K [4], and in gravitational conditions ranging from microgravity to hypergravity [2], [5], [6]. Their simple structure additionally lends itself well to miniaturization. Several examples of heat pipes constructed from etched silicon exist [6]–[11], with flat profiles of 10 cm^2 or less.

Oscillating heat pipes represent a comparatively recent innovation within the field of heat transfer, being first introduced in the 1990s by Akachi [12]. These devices are similar to conventional heat pipes in that they utilize the evaporation and condensation of a contained fluid in order to passively transfer heat. Unlike traditional heat pipes, however, oscillating heat pipes do not use a wick to return condensed liquid to the evaporator section of the heat pipe. Instead, the pipe forming the heat pipe is wound back and forth several times between the evaporator and condenser as seen in Figure 1. These tubes are sized near or below the capillary length of the working fluid, leading to a mixed distribution of liquid and vapor slugs within the heat pipe. As heat is applied to the evaporator, vapor plugs form or grow, increasing the local pressure. Simultaneously, condensation within the cooled section of the heat pipe reduces the pressure within this section. The resulting pressure differential drives liquid slugs from the evaporator to the condenser. The inclusion of

several turns within the heat pipe results in local pressure minima and maxima that vary with time and location within the heat pipe, leading to chaotic, oscillating motion of the fluid slugs.

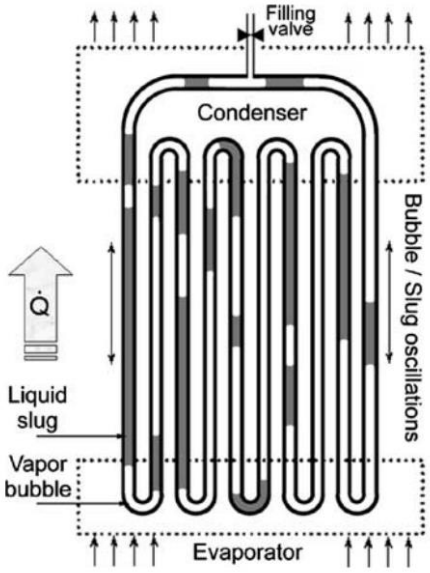

Figure 1: Schematic of a closed loop OHP [13].

Oscillating heat pipes are often further classified as being open or closed loop. In the former, the meandering tube comprising the heat pipe is terminated at either end. In the latter, the two ends of the tube are connected in order to form a continuous liquid channel as is shown in Figure 1. Most studies comparing these two designs have found that the circulating flow allowed by the closed loop design leads to an increase in heat transfer [13], [14]. However, comparisons made by Jun and Kim have indicated that for micro-OHPs open loop heat pipes can provide better performance in disadvantageous orientations while retaining comparable performance to closed loop heat pipes in normal conditions [7]. Additional experiments focused solely on closed loop OHPs have indicated that the thermal resistance of these devices is minimized when the flow is circulating [15], which would support the theory that a design allowing such flow would serve to improve heat transfer.

1.1. OHP Principle of Operation and Important Parameters

While OHPs are structurally more simple than conventional heat pipes, the fluid dynamics and thermodynamics controlling their performance are in general quite complex. As mentioned above, oscillating heat pipes consist of a meandering tube with a cross section near to, or lower than, the capillary length of the working fluid. Due to the size of the tube, capillary forces dominate gravitational ones locally and the fluid distributes into alternating liquid and vapor sections. Evaporation within the heated section and condensation within the cooled cause pressure variations between adjacent slugs, driving movement within the fluid. The inclusion of multiple connected turns between the evaporator and condenser results in multiple pressure perturbations within the heat pipe, which serves to prevent fluid motion from stagnating within a driven heat pipe [16]. The current consensus on the effect of various parameters on OHP performance is summarized within the following sections.

1.1.1. Fluid Properties

While there is not yet a widely accepted figure of merit for oscillating heat pipes, the fluid properties most commonly considered relevant for OHPS are surface tension, latent heat, specific heat, viscosity, and rate of change of saturation pressure with temperature, dP_{sat}/dT [17]. Some sources expand this list to include the contact angle hysteresis for the fluid/wall combination [18].

Surface tension serves to retard fluid flow as the added capillary forces tends to dampen fluid movement. However, a higher capillary limit allows the heat pipe to be constructed with a larger channel diameter. This in turn allows more fluid transfer and a decrease in the effect of viscous losses, increasing the overall heat transfer. Overall, the

effect of surface tension is to provide an effective minimum and maximum channel diameter. This may be expressed as [18]

$$0.7\sqrt{\frac{\sigma}{g(\rho_l-\rho_v)}} \leq D \leq 1.84\sqrt{\frac{\sigma}{g(\rho_l-\rho_v)}}, \tag{1}$$

where σ represents surface tension, g gravitational acceleration, D the channel diameter of the heat pipe, and ρ_l and ρ_v the density of the liquid and vapor, respectively. It should be noted that the coefficient on the right side of equation (1) is alternately provided as 2 rather than 1.84 [19]. Heat pipes with a channel diameter larger than this will not maintain the single-phase fluid and vapor slugs characteristic of OHPs, producing a device that is in effect several inter-linked thermosyphons. Conversely, it has been observed experimentally that heat pipes with a channel diameter too small for the working fluid will not operate [13], [19]. It should be noted that the maximum and minimum diameters suggested by this equation vary with temperature. The diameter should therefore be verified at the extremes of the expected operational temperatures for the heat pipe.

While latent heat is generally agreed upon as an important parameter in fluid selection, its reported effect on heat pipe performance is inconsistent. As phase change drives fluid motion within an OHP a lower latent heat value allows more vigorous motion for a given heat flux. However, it also results in less heat being absorbed or released per unit mass of working fluid, reducing the effectiveness of latent heat transfer. Experimentally, both Ma and Faghri report that a lower latent heat results in more vigorous oscillations, aiding heat transfer [17], [20]. In an experimental study comparing the performance of several fluids Zhang additionally found that a lower latent heat aided heat pipe startup, allowing operation at lower heat fluxes [14]. This complements the result by

Taft that indicates that a higher latent heat results in a lower required wall superheat to induce boiling, and so aids heat pipe startup [18]. However, Han found that a lower latent heat resulted in dry-out at lower heat flux values [21], while Khandekar indicates that both very high and very low latent heats may degrade heat pipe performance [22]. This would suggest the existence of an optimal value, though no relation describing such is provided.

The force that drives fluid flow within an OHP is the pressure differential between the evaporator and condenser. As this pressure difference is directly tied to the saturation pressures at each end of the device, a higher dP_{sat}/dT results in a larger driving force for a given temperature difference between the evaporator and condenser. This larger driving force results in more vigorous fluid motion and heat transfer, resulting in a lower device thermal resistance.

A higher fluid specific heat allows more energy to be stored within each liquid slug for a given temperature difference, which aids sensible heating. A higher thermal conductivity aids heat penetration into the fluid, and so serves to aid in the overall heat transfer of the OHP. Fluid viscosity is primarily important to OHPs in that it retards fluid flow. As this value is decreased, fluid motion within the heat pipe becomes more vigorous, leading to an increase in heat transfer.

1.1.2. Effect of Geometry and Number of Turns

As mentioned previously, the capillary length of the working fluid serves to bound the channel diameter. Within this bound it has been reported that increasing the channel diameter leads to a decrease in the thermal resistance of the heat pipe [11], [13], [23], as well as its critical heat flux [11], [15]. This decrease in thermal resistance results both from

the larger fluid inventory allowed by the larger diameter as well as a decrease in viscous losses.

It has been noted in several papers that decreasing the length of the evaporator leads to increased thermal performance [15]. A modeling effort by Jiansheng et al. additionally found that applying the heat load to only a fraction of the OHP's tubes led to startup times 50-75% of those for heat pipes with a uniform heat load, though this concentrated load did lead to an increase in thermal resistance [24].

Increasing the number of turns within an OHP has been found to improve overall performance. In particular, early experiments by Charosensawan et al. [13] revealed that the effect of gravity was reduced as the number of turns was increased, eventually reaching a state where the OHP operation was independent of orientation. Moreover, when the number of turns was below a critical value N_{crit} the heat pipe was not able to operate without the assistance of gravity; i.e., without the evaporator placed below the condenser. For the studied heat pipes this N_{crit} was found to be 16, though no generalizable correlation was developed for this value. Jun and Kim have corroborated this decreasing influence of gravity as the number of turns in the heat pipe is increased, and additionally found that increasing the number of turns decreased the difference in performance between open loop and closed loop pulsating heat pipes [7]. Kammuang-Lue et al. have reported an increase in the maximum heat flux as the number of turns is increased, though the magnitude of the increase was not consistent between the heat pipes measured [15].

There has additionally been some research done into the effect of non-circular channel geometry. Yang et al. provided experimental results for two heat pipes with rectangular channels, as well as a comprehensive overview of the theoretical considerations

for the use of rectangular and triangular channels [23]. They noted that the sharp corners present within these shapes aided fluid wetting and increase capillary forces, allowing slug and annular flow to be sustained up to higher input powers. Additionally, they noted that this difference in capillary force makes equation (1) inappropriate to use with rectangular cross sections, though they did not provide a substitute. While direct comparisons between rectangular and circular channel cross-sections are rare, experiments by Lee and Kim have indicated that rectangular channels increase the critical heat flux of the heat pipe by up to 70% when compared with circular channels of the same hydraulic diameter [11].

1.1.3. Fill Ratio

It is generally reported that most of the heat transferred within an OHP is due to sensible heat transfer. As such, an increase in the amount of liquid provides more thermal mass with which to transfer heat. However, as phase change is the primary contributor to driving force, increasing the liquid fill percentage too far will serve to retard flow, decreasing overall heat transfer. It therefore follows that there is an optimal liquid fill ratio for a given oscillating heat pipe. There have been a number of experiments performed attempting to determine this optimum value, typically testing fill ratios ranging from 30% to 70% by liquid volume fill fraction. The majority of these studies report that the optimum fill is near 50% [19], [25]. Yang et al further reported that a fill ratio of 50% provided the highest critical heat flux out of all the values they tested [25], indicating that this fill ratio provides the greatest possible heat transfer as well the lowest thermal resistance.

1.1.4. Other Considerations

Several attempts have been made to improve the thermal performance of oscillating heat pipes by adding additional features. One of the most popular of these has been the inclusion

of a feature promoting one-directional flow within sections of the heat pipe. As mentioned above, it has generally been found that circulating flow leads to improved heat transfer performance. The inclusion of these devices serves to promote flow in one direction, and so lower the heat flux threshold required to obtain circulating flow. The most commonly used devices for this are tesla valves or check valves [17], [20], [26]. Kwon and Kim have additionally experimented with a dual-diameter design [6]. In this design the OHP was fabricated with channels of two diameters, alternating between adjacent channels. This provided a preferential capillary force in one direction, promoting circulating flow. In addition to decreasing the thermal resistance of the heat pipe when compared to a single diameter design, the authors found that the dual-diameter design's operation was not affected by heat pipe orientation.

Another common variation on the OHP design is the inclusion of features to promote boiling. Kim and Kim experimented with the inclusion of re-entrant cavities and found them both to reduce the power required for startup and the overall thermal resistance of the heat pipe [27]. They noted that larger cavities had a greater impact on startup performance, while smaller ones more were more effective at reducing thermal resistance at high heat fluxes. They further found that these two effects could be combined by the inclusion of cavities spanning a range of sizes. Qu et al. experimented with a similar design, utilizing helical micro-grooves in place of re-entrant cavities [28]. As with the re-entrant design, these micro-grooves both aided startup and reduced the thermal resistance of the heat pipe. In addition, they served as a rudimentary wick, promoting the return of liquid from the condenser to the evaporator.

Other researchers have experimented with the use of nanofluids in order to increase heat transfer [29]–[32]. The theoretical advantage conferred by these fluids is an increase in effective fluid thermal conductivity and a lower superheat required for boiling, as the nanoparticles provide additional nucleation sites. Experiments to date have shown reductions in thermal resistance of 25-60% when compared to the unaltered working fluid [31], [32]. Qu and Wu, however, have found that certain types of nanoparticles (SiO_2 in their experiment) instead decrease heat pipe performance [30].

1.2. Flow Regimes and Startup

OHP operation is characterized by several operating modes, which is dependent upon the heat flux applied. There are several studies detailing flow regimes and transitions within the literature [10], [15], [16], [33], [34], with Khandekar et al.'s analysis being perhaps the most thorough [16]. While the exact distinction made between flow regimes differs between authors, the generally described behavior is as follows, in order of increasing heat flux:

1. Startup: From rest, fluid slugs will begin to oscillate intermittently between the evaporator and condenser. Fluid motion within this regime is not constant, and there is no overall flow direction. As fluid slugs move from the evaporator to the condenser they decrease the overall temperature difference between the two. This decreased temperature difference leads to a lower pressure difference, leading to slowed or stopped flow. Once the flow has stopped the evaporator begins to climb in temperature once again, and the process is repeated.
2. Full Flow: As the heat flux or temperature difference is further increased, fluid flow becomes continuous. At this stage an overall flow direction is often noted.

3. Annular Flow: As the heat flux is further increased the flow within the heat pipe transitions to annular flow. Several authors have noted an intermediate step, where flow from the evaporator to the condenser is annular with slug flow returning fluid from the condenser back to the evaporator.
4. Dry-Out: As with conventional pipes, the heat transfer limit of the OHP is imposed by a dry-out condition, in which liquid is evaporated from the heated section more quickly than it may be returned. As with conventional heat pipes, this stage is accompanied by a sharp increase in the thermal resistance of the OHP [11], [25].

Heat pipe startup is typically defined as the point at which oscillations begin. For this to occur the pressure differential between the evaporator and condenser must be large enough to overcome the capillary forces holding the fluid slugs in place. During this startup phase the thermal resistance of the heat pipe is quite large, as heat is only removed by conduction through the support structure and heating of the liquid. Once a critical evaporator temperature is reached fluid motion begins, and the overall resistance of the device drops precipitously. This drop in resistance is often accompanied by rapid drop in evaporator temperature [19]. Of further note, the evaporator temperature typically increases nearly linearly with heat flux prior to heat pipe startup. Once the heat pipe is operating, however, the temperature difference between the evaporator and condensor is nearly constant with heat flux [33].

There is currently no reliable correlation for the prediction of the time and heat flux required for startup. This is due primarily to the large number of factors affecting startup, several difficult to predict, and the uncertainty in their relative importance. Khandekar et al., for example, observed that even for the same heat pipe oscillations may begin nearly

instantaneously upon applying heat or may require in excess of 15 minutes to appear [16]. It is thought that this variability is due to the impact of the initial fluid distribution within the heat pipe, which is effectively random.

1.3. Heat Transfer Mechanism

There are two mechanisms responsible for transferring heat within an oscillating heat pipe. The first of these, latent heat transfer, refers to the energy absorbed and released by the fluid as it evaporates and condenses and is the primary method by which traditional heat pipes transfer heat. The second mechanism, generally referred to as sensible heat, involves the transfer of heat by warming and sub-cooling of the single-phase liquid slugs as they move from the evaporator to the condenser.

One of the outstanding questions concerning OHPs is the relative contribution of these two mechanisms. To date, OHP modeling attempts have generally indicated that sensible heat dominates the overall heat transfer through the heat pipe, typically listed as accounting for greater than 80% of the overall heat transfer [9], [35]–[39]. Following this view, the purpose of phase change within the heat pipe is primarily to drive flow. Mehta and Khandekar have indicated that the turbulence caused by the moving vapor bubbles increases convection in their wake, suggesting that the vapor also aids sensible heat transfer [40]. However, at least one modeling attempt has instead reported that heat transfer is dominated by latent heat [41]. Additionally, at the time of this writing the sole experimental attempt to determine the dominant heat transfer method indicated that roughly 74% of heat transferred within the evaporator and 66% of the heat transferred within the condenser of the heat pipe studied was due to evaporation and condensation [42].

2. Experimental Overview

The primary purpose of this experiment was to provide a better understanding of the heat transfer mechanism within an oscillating heat pipe. This was done using an optical technique pioneered by Al Hashimi et al [43] utilizing temperature sensitive paint (TSP). This paint is excited by ultraviolet light and re-radiates in the visible spectrum with an intensity dependent upon the temperature of the TSP. Applying this paint over an area allowed continuous heat transfer and temperature measurements across the entire face of the OHP.

2.1. Experimental Theory and Setup

The OHP system was set up as shown in Figure 2. Here, TSP was spread onto a 12.7 μm thick stainless steel shim and attached to the bottom of a sapphire plate using a 50 μm layer of adhesive. Additional dots of TSP, each 1 mm in diameter, were applied directly to the back of the sapphire in a 10 mm x 10 mm grid, with a 200 nm layer of germanium underneath these dots to provide an optically opaque barrier. The thickness of the TSP layers was found to be 1-2 μm by Al Hashimi et al. [43], whose technique was copied here. It was therefore assumed that the thicknesses of the TSP layers created here were the same, though this was not verified. After application of these dots, the combined assembly was placed onto a transparent acrylic block with heat pipe channels cut into its surface. A gasket placed in between the heat pipe channels provided the seal between the acrylic and TSP stackup. The TSP stackup thus served as the top surface of OHP's channels, with the stainless steel shim in direct contact with the working fluid. Heat was applied and removed at the top surface of the sapphire to ensure that all heat transferred into or out of the heat pipe was transferred through TSP and adhesive. UV light was shone on the UV transparent

sapphire covered side of the heat pipe and the resulting visual re-radiation of light was recorded by a visual camera. Simultaneously, the acrylic side of the heat pipe was illuminated using white LEDs and the fluid motion captured using a second camera.

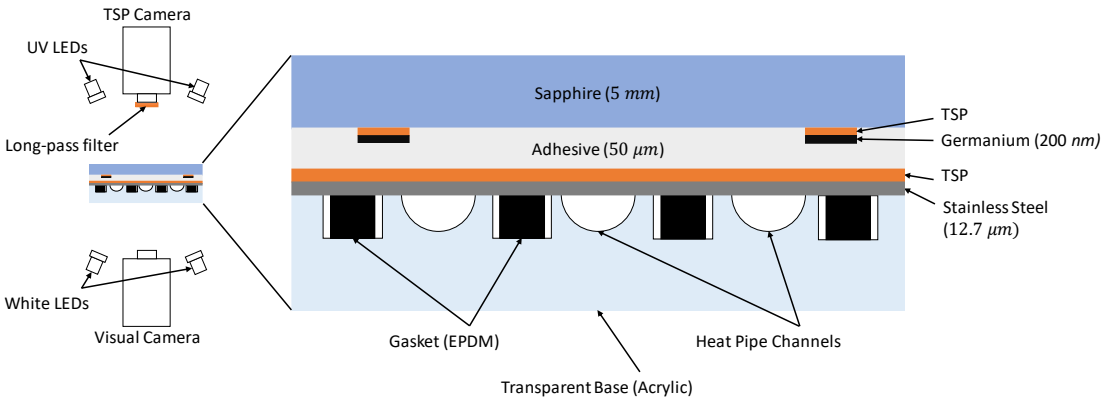

Figure 2: Heat pipe cross section and camera configuration (not to scale)

The TSP applied to the stainless steel shim was in good thermal contact with the working fluid of the OHP, and so its temperature could be taken to be the same as that of the working fluid where it contacts the wall of the channel. The TSP dots were used to measure the temperature of the sapphire/adhesive interface and interpolated to provide an estimate of the temperature distribution across the entire surface of the high conductivity sapphire. The heat flux was then calculated as a simple one-dimensional heat transfer problem using the known thickness and thermal conductivity of the 50 μm adhesive. This method did not account for heat transfer between the working fluid and the acrylic, which was assumed to be negligible in comparison to heat transferred to the sapphire. This assumption is examined in more detail in section 3.3.

Heat was applied to the top of the sapphire using a transparent vapor-deposited ITO heater approximately 11 mm in height by 36 mm wide. This ITO layer, 200 nm in thickness, was deposited directly onto the sapphire using an AJA ATC 1800 sputtering

unit. Copper wires were attached to this heater using silver paint and routed to the Tenma 72-2715 power supply used for heating. A water-cooled condenser block was placed at the top of sapphire, slightly offset from the channels to prevent it from obscuring the camera's view of the TSP. The condenser inlet temperature was measured using a T-type thermocouple. Six UV (410 nm wavelength) LEDs were used to illuminate the TSP, while four white (CCT of 3700 to 3900 K) LEDs illuminated the fluid motion. TSP visualization was performed using a Photometrics Prime monochrome camera with 16 bit depth per pixel. Visual data was recorded with a Sentech STC-MBCM200U3V monochrome camera using a bit depth of 8 bits per pixel. Both cameras were connected to a Velleman PCSGU250 oscilloscope and function generator to allow simultaneous triggering. Triggering was performed using a square wave at 200 Hz, providing a time resolution of 5 ms. Exposure time was set to 0.5 ms for the visual data, and 4 ms for the TSP.

Three crosses were inscribed on the stainless steel on the underside of the TSP stackup in order to allow locations to be calibrated between the two cameras. These crosses may be seen in the raw captured images shown in Figure 3. Note that here the visual image has been flipped from left to right so that the positive x axis is consistent between images. For a given coordinate in the visual image, (x_{visual}, y_{visual}) the corresponding location on the TSP image was determined using the equations

$$x_{TSP} = \left(x_v - x_{v,0}\right)\frac{x_{TSP,1} - x_{TSP,0}}{x_{v,1} - x_{v,0}} + x_{TSP,0}, \tag{2}$$

$$y_{TSP} = \left(x_v - x_{v,0}\right)\frac{y_{TSP,1} - y_{TSP,0}}{y_{v,1} - y_{v,0}} + y_{TSP,0}, \tag{3}$$

where the *v* subscript refers to a coordinate on the visual data (Sentech) and *TSP* a point on the TSP image (Prime). Points 0 and 1 are common locations between the two images. For the x direction point 0 was taken as the leftmost point in the left cross in Figure 3, while point 0 was taken as the rightmost point in the top right cross. For the y direction the topmost point in the top right cross was used for point 0, while the topmost point of the lower right cross was used for point 1. The vertical length of the largest cross was used to ensure the two images were rotationally aligned. In both images the x coordinate for the top-most point on the large cross was the same as the x coordinate of the bottom-most point on the same cross, and so it was assumed that the images were not rotated relative to one another.

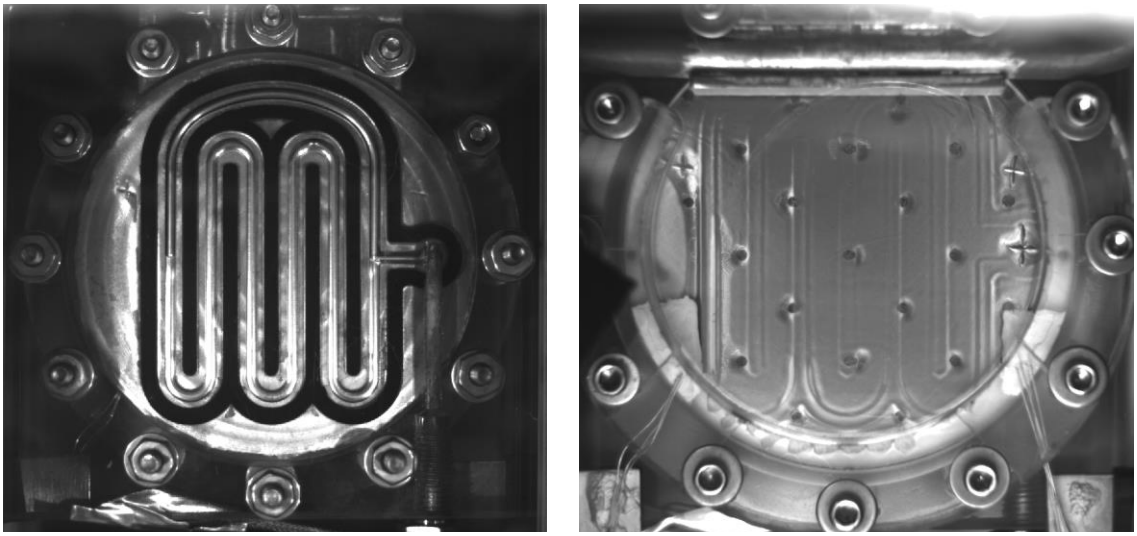

Figure 3: Visual (left) and TSP (right) images. Crosses used for coordination may be seen at left and at top right. Visual image is flipped left to right in order to coordinate locations.

2.1.1. TSP Production, Application, and Calibration

The TSP used for this study was composed of Ruthenium tris (1, 10-phenan-throline) dichloride mixed with polyacrylic acid. Following the formula used by Al Hashimi et al

[43] the TSP mixture was created from 40 mg of Ruthenium compound combined with 100 mg of polyacrylic acid. This was then suspended within 0.5 mL of isopropyl alcohol and spread across the desired surface using a size 2 Mayer rod.

The intensity response of the TSP must be converted to a temperature prior to analysis. To determine the relation between temperature and measured intensity the heat pipe was brought to a fixed temperature, illuminated, and then the TSP facing camera set to record 1000 images. These images were then averaged and the resulting intensity at each pixel used as the value representing the calibration temperature. This was performed for five temperatures spanning the expected operational range of the heat pipe. The intensity of the light emitted from the TSP decreased monotonically with increasing temperature as illustrated in Figure 4 for a few representative pixels. Previous experiments using this TSP compound have found that a quadratic function adequately fits the data [44], and so a second order fit was applied to these data points. Individual coefficients were calculated for each pixel in the image to account for differences in lighting, TSP thickness, and other factors that might cause variations in the intensity from pixel to pixel. Figure 4 shows the measured data alongside the fit curves for five representative pixels.

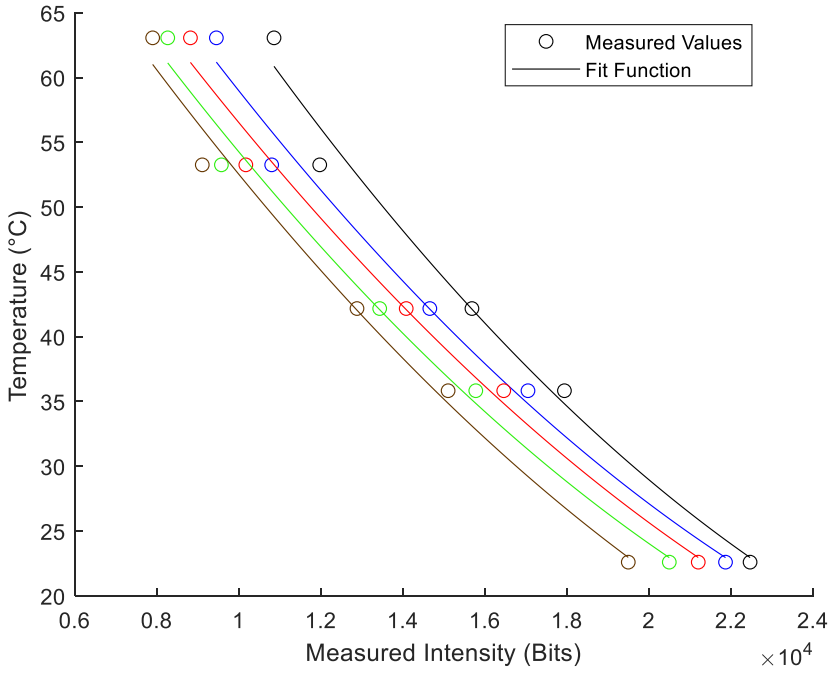

Figure 4: Fit function for five representative pixels

TSP calibration was performed in earlier experiments by varying the temperature of the working fluid in order to control the temperature of the TSP [43], [44]. This was not possible for the oscillating heat pipe apparatus. Instead, the heat pipe was placed within an insulated enclosure along with a finned aluminum block to which several heaters were attached (Figure 5). A fan was placed immediately underneath this block to bring the air within the enclosure to a uniform temperature, and the combined assembly stood off approximately 5 cm from the table to allow airflow from underneath. Finally, a foam pad was placed underneath the entire assembly both to reduce gaps at the base of the enclosure and to dampen vibration caused by the fan. Acrylic windows were placed within the enclosure, sealed to its walls using silicone adhesive, to provide the cameras a view of the heat pipe. The heater block was warmed to a temperature 20°C to 30°C above the intended calibration point, and the entire enclosed system was allowed to warm until thermal

equilibrium was achieved. Once at thermal equilibrium the heat pipe was illuminated and a calibration point recorded.

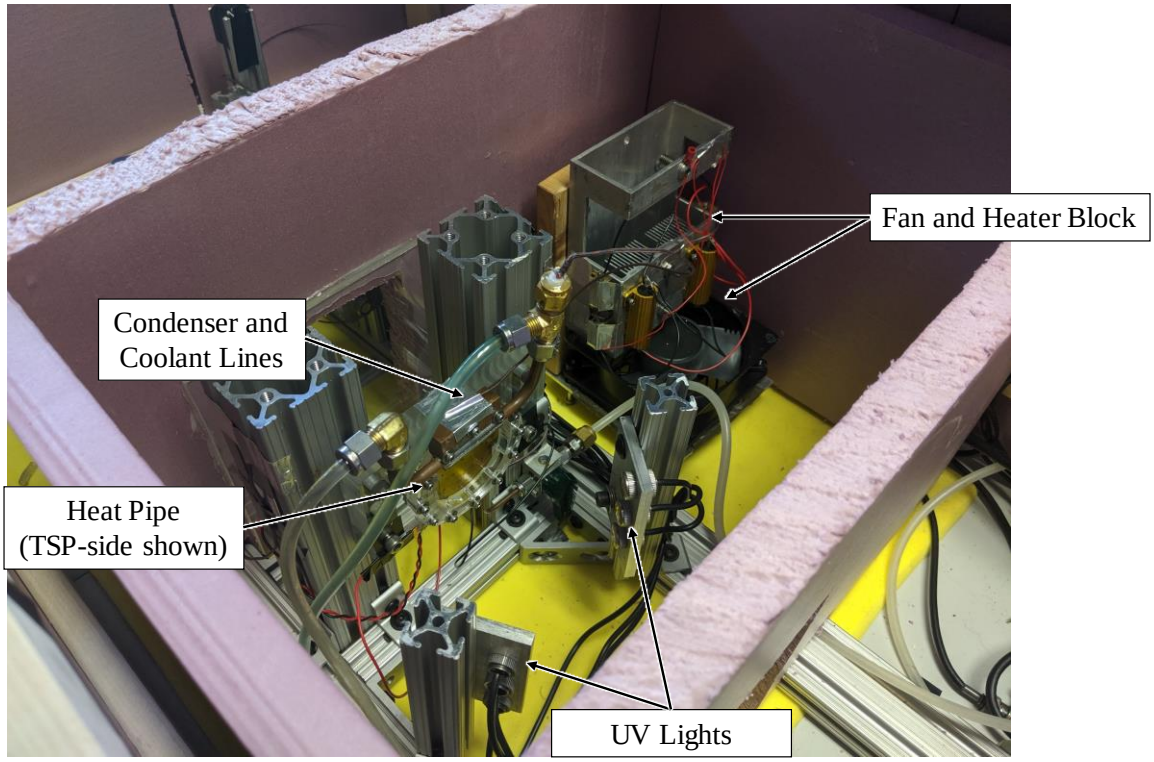

Figure 5: Heat Pipe within heated enclosure.

Temperatures were measured throughout the enclosure using five type T thermocouples. The mean temperatures for each calibration may be found in Table 1 along with the standard deviation between each of the five thermometers.

Table 1: Calibration Temperatures

Calibration Temperature (°C)	Standard Deviation in Temperature (°C)
22.6	0.12
35.8	0.17
42.2	0.31
53.3	0.44
63.1	0.71

2.1.2. TSP Response Time

The time-response of the TSP temperature measurement was dependent upon the time-response of the 12.7 μm stainless steel shim in contact with the working fluid. As this time response is important to the subsequent analysis, it is considered briefly here. The following equation was used to provide an approximate thermal time constant:

$$\tau_0 = \frac{\delta_0^2}{\alpha}, \tag{4}$$

where τ_0 represents the thickness of the material and α its thermal diffusivity. For this measurement a value of 4.05 mm^2/s was used for the thermal diffusivity of the stainless steel. This provided a thermal time constant 40 μs. As this is two orders of magnitude smaller than the camera time resolution of 5 ms it was assumed that the temperature time resolution of the data was the same as that of the camera.

The heat transfer calculation assumed a linear temperature distribution within the acrylic adhesive layer. As such, the time resolution of the heat transfer data was dependent upon the characteristic time required for this layer to reach steady state. The adhesive manufacturer, 3M, does not provide density, thermal conductivity, or specific heat data for

this material. The thermal conductivity was measured to be 0.12 W/m-K (as detailed in section 2.2) while the density and specific heat of PMMA were used to provide an approximate time constant. Using this thermal conductivity value with a density value of 1190 kg/m^3 and a specific heat of 1460 J/kg-K provided a thermal diffusivity of 0.08 mm^2/s for the adhesive. Placing this value of α within equation (4) provided a thermal time constant of 45 ms, which served as the approximate time response of the heat transfer data. While this value could have been decreased by using a thinner or higher conductance adhesive, both changes would have served to decrease the temperature difference across the adhesive and thus the accuracy of the heat transfer measurement. The 50 μm adhesive used here was deemed to provide an acceptable trade-off between these two factors.

2.1.3. Heat Pipe Geometry

The heat pipe channels were semi-circular with a short rectangular section at the interface with the stainless steel. The channel width and diameter of the semi-circular section were both 1.6 mm, and the channel depth was 1.0 mm, resulting in a hydraulic diameter of 1.2 mm. Across the expected heat pipe operational range of 20 to 80°C equation (1) would indicate allowable minimum and maximum hydraulic diameter limits of 0.7 mm and 1.4 mm, respectively. The heat pipe had six channels, each with a straight length of 31.9 mm. The heat pipes primary dimensions are given in Figure 6. An EPDM gasket, laser cut to match the heat pipe's profile, was used to provide a seal between the stainless steel shim and the acrylic base. To provide pressure for the seal, an acrylic clamp was placed on top of the sapphire and bolted to the base with twelve 4-40 screws. These screws were lubricated and torqued to 2 in-lbs with a calibrated torque wrench, providing a theoretical clamping force of 1200 lbf across the gasket.

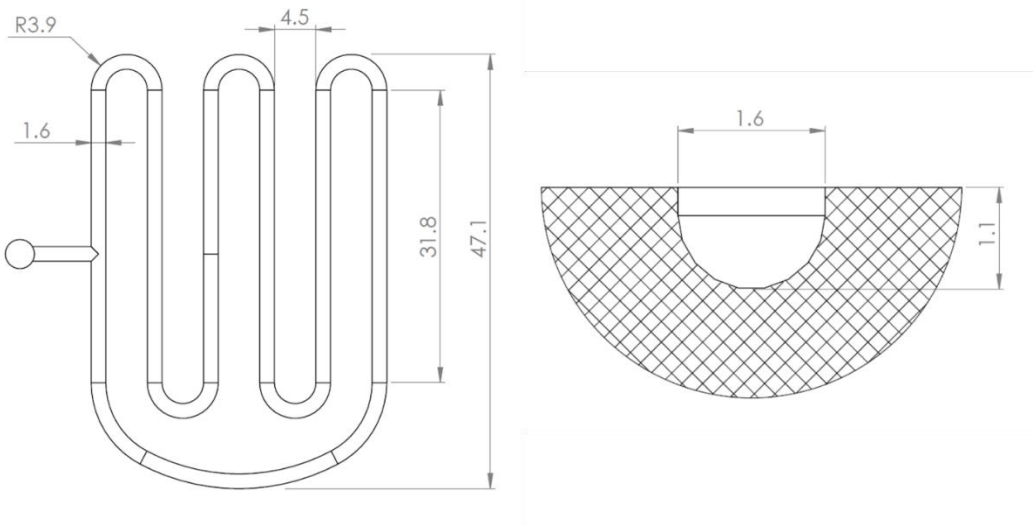

Figure 6: Heat pipe channel geometry. All measurements are in mm.

2.1.4. Working Fluid

HFE 7000 ($C_4F_9OCH_3$) was chosen as the working fluid. The room temperature values of the relevant properties for this fluid are shown in comparison to other common working fluids in Table 2. HFE 7000 has a relatively large $(dP/dT)_{Sat}$ across the operational temperature range used here, as may be seen in Figure 7. The values used for $(dP/dT)_{Sat}$ in this figure have been derived from the 3M provided saturation curves for HFE 7000 and 7100 [45], [46], and the Antoine equation for the remaining three, the parameters for which were taken from the NIST Chemistry Webbook [47]–[49]. In comparison to the other considered fluids HFE 7000 additionally has the advantage of low viscosity, low latent heat of vaporization, and high density but has comparatively low thermal conductivity and

specific heat. This fluid was also chosen due to its near room-temperature boiling point, inertness, and low toxicity.

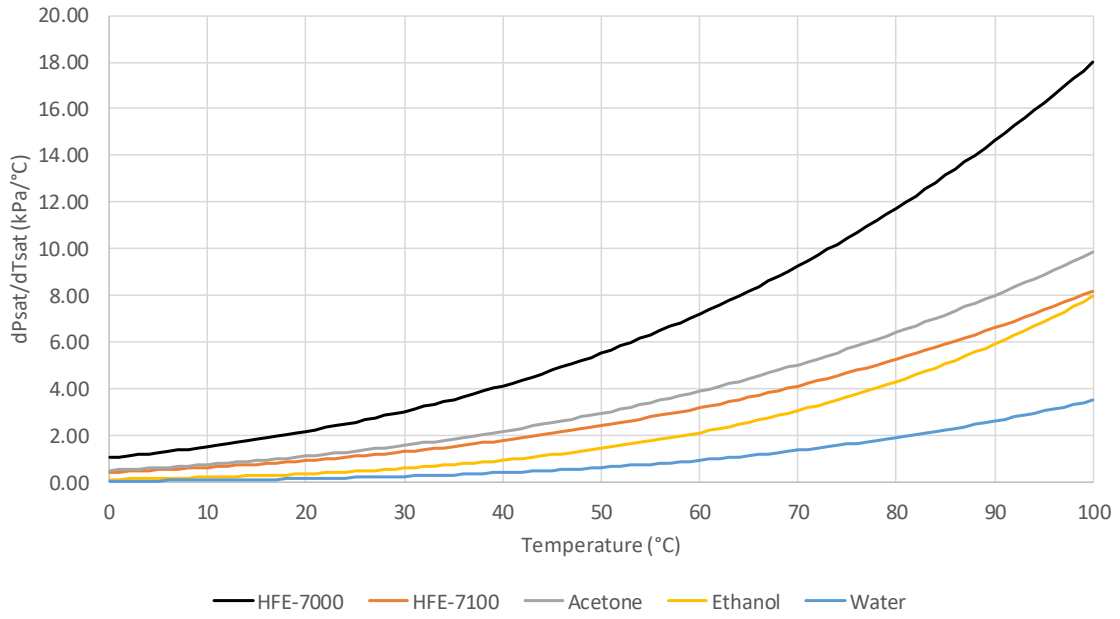

Figure 7: Comparison of saturation pressure gradient with temperature for several fluids [45]–[49].

Table 2: Room temperature thermodynamic properties of commonly used working fluids

Fluid	Liquid Density (kg/m^3)	Liquid Specific Heat (kJ/kg-K)	Liquid Thermal Conductivity (W/m-K)	Surface Tension (mN/m)	Liquid Viscosity (µPa-s)	Latent Heat (kJ/kg)
HFE 7000 [45], [50]	1418	1.30	0.075	12.3	467	142
HFE 7100 [50], [51]	1529	1.18	0.069	13.8	580	112
Acetone [20], [52]	790	2.16	0.181	23.7	323	552
Ethanol [20], [52]	800	2.40	0.179	22.8	1020	1,030
Water [20], [52]	999	4.18	0.602	72.9	1000	2,454

2.1.5. Filling Procedure

The plumbing schematic used to fill the heat pipe is shown in Figure 8. Prior to filling the working fluid must be degassed, a process performed here in three steps. Beginning with all valves closed, the pump was turned on and V1 cracked to pull gas from the top of the

reservoir. This was continued for several minutes until P_1 registered a pressure near the vapor pressure of the working fluid at room temperature, equal to 65 kPa for HFE 7000. Second, V1 was closed and the reservoir heated until the internal pressure was above atmospheric pressure, typically to a value between 70 and 100 kPa gauge. Finally, V2 was cracked and the pressure allowed to fall to roughly 35 kPa gauge before closing V2. This heating, pressurization, and venting was then repeated several times prior to fill.

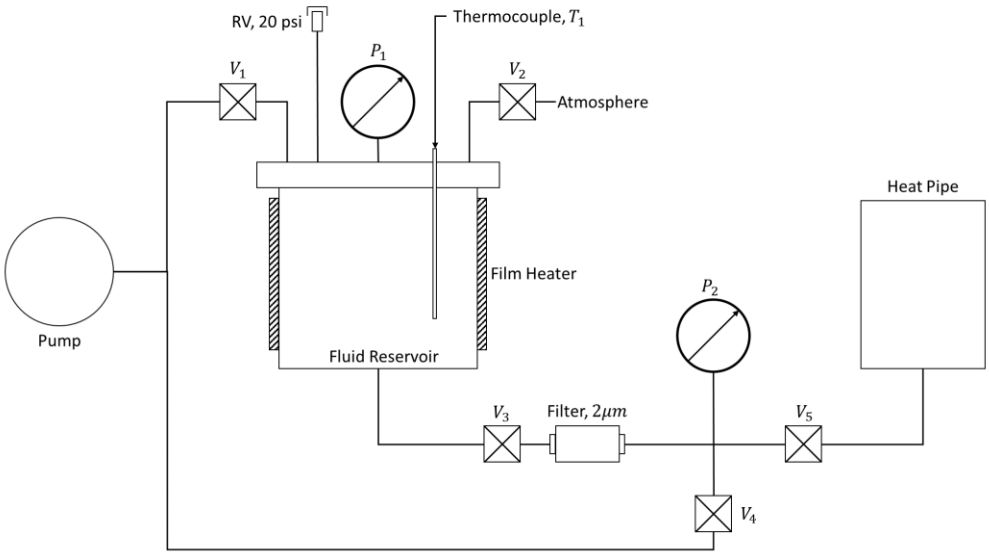

Figure 8: Plumbing schematic for heat pipe fill

The heat pipe fill was performed immediately following degassing. Beginning with all valves shut, the filling procedure was as follows:

1. Open V_4 and V_5. Turn on the pump and evacuate the heat pipe.
2. Warm the fluid reservoir until P_1 registers a temperature between 70 and 100 kPa gauge.
3. Close V_4.

4. Crack V_3 while monitoring the fill level of the heat pipe. Allow the heat pipe to fill to the desired level and close V3.
5. Allow the fluid within the heat pipe to come to thermal equilibrium.
6. Crack V_3 to allow more fluid into the heat pipe if level has fallen below the desired value.
7. Repeat steps 4 and 5 until fluid level is at desired value at room temperature.
8. Close all valves.

Pumping of the heat pipe in step 1 was performed for a period of at least 30 minutes to ensure complete evacuation. The heat pipe was filled to approximately 50% liquid by volume during the filling procedure using simple visual estimation from the camera feed. This was later confirmed to be 52% using the visual data obtained during testing.

2.2. Adhesive Thermal Conductivity Measurement

The thermal conductivity of the acrylic adhesive was required for the heat pipe heat transfer measurement, as detailed in the experimental procedure section. As 3M does not provide this property of the adhesive it was measured by creating a heat flow across a sample of the adhesive and measuring the temperature difference across it (Figure 9). Four layers of 50 μm adhesive were stacked upon one another in order to increase the overall temperature difference for a given heat flux. Heat flux was measured using a FluxTeq PHFS-09e sensor with a resolution of 0.2 W/m^2. Temperature measurement was performed using two type E thermocouples, each 5 μm thick. Approximately 100 W of heat was applied to the top copper interface plate and was removed by a heat exchanger connected to a chiller at the base. Foam was placed around the outside of the adhesive to reduce heat loss to convection.

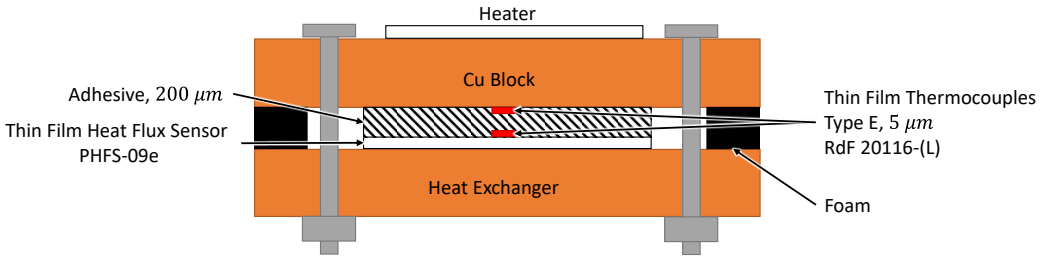

Figure 9: Thermal conductivity measurement schematic

The thermocouples were calibrated at 0°C, 100°C, and 23°C. The calibration at the first two of these points were performed by placing the thermocouples within a deionized water bath, filling it with ice, and then bringing the system to boiling. In order to calibrate at a third point a platinum resistance thermometer (PRT) (Lakeshore part number PT-102) was placed in the bath with the thermocouples and calibrated at 0°C and 100°C. This PRT was then used to determine the temperature of the third, room temperature calibration point. A linear fit of these three data points was then used to determine the emf-temperature relationship for each of the thermocouples. An example is shown in Figure 10.

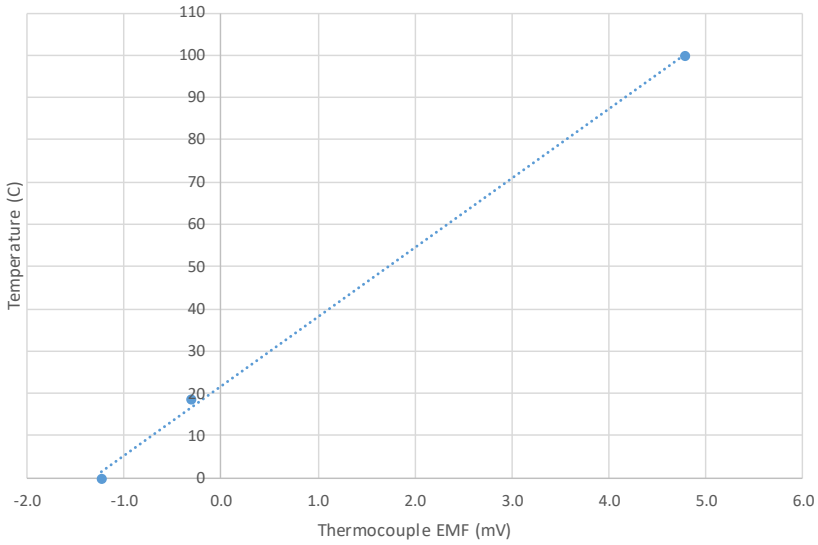

Figure 10: Thermocouple calibration

The test was performed with a heat flux of 6.58 kW/m^2 through the adhesive, resulting in a temperature gradient of 11.6°C across the 214 μm sample. From this the thermal conductivity was determined using the equation

$$k = \frac{q'' L_{adhesive}}{\Delta T} \tag{5}$$

where k is the thermal conductivity, q'' the measured heat flux, $L_{adhesive}$ the thickness of the adhesive, and ΔT the temperature difference between the two sides of the adhesive. Using this equation, the experimentally determined thermal conductivity used for analysis was 0.12 ± 0.01 W/m-K.

2.3. Heat Transfer Uncertainty Analysis

The uncertainty of a given parameter may be estimated using the equation

$$\mu_\sigma = \sqrt{\sum_{\mathrm{i}} \left(\frac{\delta \sigma}{\delta \epsilon_{\mathrm{i}}} \mu_{\epsilon_i} \right)^2} \tag{6}$$

where μ represents the error in the subscripted term, σ is the parameter whose error is to be calculated, and ϵ is a parameter that affects the evaluation of σ. For temperature, the parameters affecting the error were determined to be the thermocouple error, the camera noise, and the resolution error.

Camera noise and its effect on temperature was analyzed using the calibration data. For each calibration run, 1000 images were taken over several seconds with the heat pipe held at a fixed temperature. Each set of 1000 images may therefore be used to determine the noise at each pixel independent of changes due to temperature variation. To perform noise analysis the temperature-intensity function described in the calibration section was

applied to each of the calibration data-sets to obtain the predicted temperature for each pixel for each of the 1000 images.

The variation in predicted temperature for a single pixel may be seen in Figure 11 with a normal fit superimposed. The predicted temperature follows a normal distribution with its center at the calibration temperature. The median standard deviation for the pixels covering the heat pipe channels is summarized in Table 3 at each of the calibration temperatures. The standard deviation does not appear to have any temperature dependence, and has a maximum value calculated at 0.6°C. As 95% of all points are expected to fall within two standard deviations of the mean, the error due to camera noise was taken to be equal to ± 2σ, or ± 1.20°C.

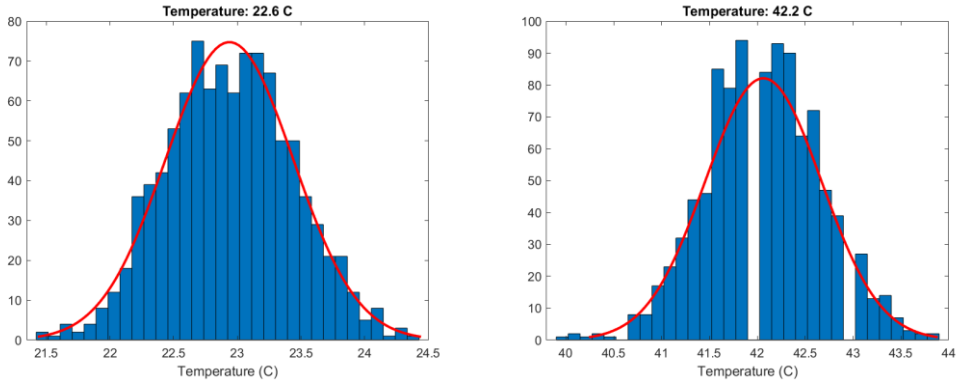

Figure 11: Histogram of temperatures predicted by intensity-temperature fit for one pixel for 1000 images taken at 22.6°C and 42.2°C.

Table 3: Standard deviation in predicted temperature at each calibration point

Calibration Temperature, °C	Standard Deviation, °C
22.6	1.01
35.8	1.17
42.2	1.20
53.3	1.19
63.1	1.15

The extension grade T-type thermocouples used here have a standard error of 0.5°C. The camera used for acquisition has a resolution of 16 bits per pixel, which provides a resolution of ±0.0035°C at the maximum and minimum calibration temperature. Using equation (6) these values provide an overall error in temperature at each pixel of ±1.3°C.

Analysis of the heat flux error required a value for the error in the thermal conductivity. As indicated by equation (5) the values contributing to this value were the heat flux, adhesive thickness, and temperature difference. Per the calibration from FluxTeq the accuracy of the PHFS-09e heat flux sensor was 5% of reading. The thickness of each of the four pieces of adhesive used to create the overall stack were measured independently, each using a differential measurement. The thickness of the adhesive and its plastic backing were measured, then the adhesive removed and the thickness of the backing measured by itself. As the accuracy of the micrometer used for measurement was 1 μm, the RMS error for the eight individual measurements used to determine the total thickness was 2.8 μm.

The standard deviation in the calibration readings was used to determine the thermocouple accuracy for the conductivity measurement. At freezing and boiling the

standard deviations were 0.05°C and 0.23°C, respectively, for the thermocouple with the largest variance in signal. The temperature accuracy was thus taken to be twice the largest standard deviation, or 0.46°C. This resulted in an overall error in thermal conductivity of 0.01 W/m/K using equation (6).

The heat flux was calculated using the equation

$$q'' = \frac{k(T_{sapphire} - T_{TSP})}{L} \quad (7)$$

for heat flux q'', adhesive thermal conductivity k, and thickness L. $T_{sapphire}$ and T_{TSP} represent the local temperatures of the sapphire and TSP touching the working fluid, respectively. Thus, errors in the adhesive thermal conductivity and thickness, as well as the temperatures of the sapphire and TSP, all contributed to the error in q''. However, errors that affected both temperatures equally, such as the thermocouple error in calibration, cancel within equation (7) and so did not contribute to $\mu_{q''}$. The error was difficult to calculate in advance, however, as the derivative terms in equation (6) depend on the temperature difference between the sapphire and the working fluid. In order to provide a bounding estimate, the largest observed value was used here. With 10 W of power applied to the heat pipe a temperature difference of up to 6.5°C was observed between the sapphire and TSP layer. As detailed above, the thickness was determined using a differential measurement with a micrometer of resolution 1 μm. As only one 50 μm sheet was used for the heat pipe test there were two thickness measurements made, giving an overall error in thickness of 1.4 μm. This provided a bounding error in q'' of ±4.1 kW/m^2.

2.4. Experimental Procedure

The heat pipe was filled immediately prior to data acquisition. In preparation for testing the chiller temperature was set to 25°C, with the value at the condenser block inlet typically within 1°C of this value. Once the chiller stabilized, a power of 2.5 W was applied to the heat pipe and the system allowed to dwell for at least 15 minutes to allow the heat pipe to reach-quasi steady state. Once at quasi-steady state two acquisition runs were taken, each of 1000 frames at a speed of 200 Hz. Following acquisition, the applied power was increased to a setpoint of 5 W, the heat pipe allowed to dwell for an additional 15 minutes at this new power, and four additional acquisition videos taken. This process was then repeated for heater setpoints of 7.5 W and 10 W. Following the measurement at 10 W, the heater power was stepped down in 2.5 W increments to a final value of 2.5 W, with 2 videos taken at each setpoint resulting in a total of 14 videos. The actual applied powers were 2.8, 5.1, 7.6, and 10.1 W as power was increased, and 7.6, 5.2, and 2.6 W as it was decreased. Applied powers greater than these were attempted with previous iterations of the heat pipe, but frequently led to burnout of the heater.

The camera triggering circuit was prepared prior to heat pipe startup but was left unpowered. For each video the Photometrics and Sentech cameras were programmed to take 1000 images, one on each rising edge registered on the triggering circuit. Once both cameras were watching for triggers, the triggering circuit was powered and acquisition begun. The white light LEDs were left on throughout testing. The UV LEDs, however, were only powered immediately prior to each acquisition run and turned off following to limit photo-bleaching of the TSP.

3. Data Conversion and Post-Processing

3.1. Image Processing

Each frame provided by the Photometrics Prime was 666 x 837 pixels in size, each pixel with a bit depth of 16. As mentioned above, calibration was performed on a per-pixel basis. Following acquisition this calibration was applied to each pixel in each frame to provide an overall temperature map. The temperature of each TSP dot was then averaged to provide a representative sapphire temperature at its center. A 2D linear interpolation was then used between these points to provide the sapphire temperature map, as shown in Figure 12. With the adhesive properties known, the heat flux at each pixel was then calculated from this temperature difference.

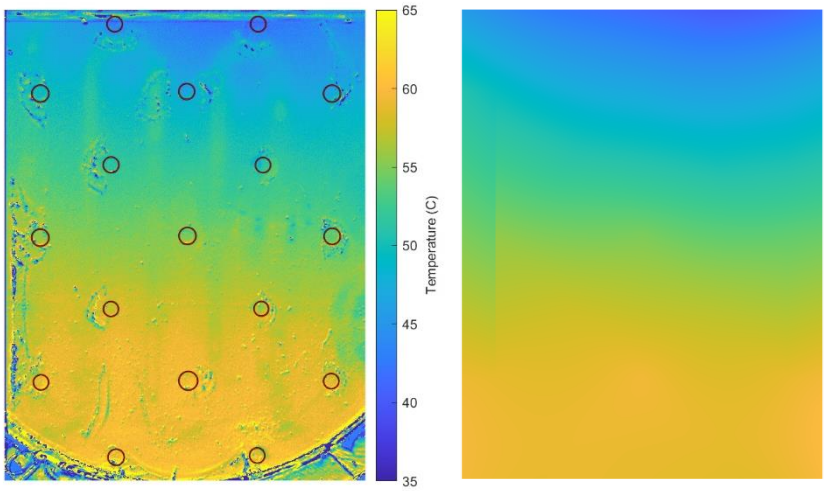

Figure 12: Sample sapphire temperature interpolation (right). Temperature image used for interpolation shown at left with dots (used for interpolation) highlighted in red.

3.2. Bias Adjustment

Examination of the heat flux data revealed an apparent cold bias – the areas of the heat pipe that should have been adiabatic (such as the locations overtop the gasket) showed an

apparent value of -1 to -3 kW/m2, which was interpreted to represent a bias error within the heat transfer data. In order to determine the magnitude of this bias, an analysis was performed to estimate the mean heat transfer value over a known adiabatic section of the heat pipe. The area covered by the gasket was chosen as the adiabatic section as it represents an easily identifiable zone spread across the entire viewed face in which no heat transfer should theoretically take place.

This analysis was performed by creating a bitmask of the regions of the heat pipe covered by the gasket. This mask was then applied to the heat flux data, averaged along the time dimension, and the mean resulting value used as the heat flux bias. Areas in which the TSP was obscured, such as by the condenser block and the acrylic clamp, were removed from the mask prior to its application. Areas covered by TSP dots or in which the TSP was damaged were likewise removed. The area used for this analysis, along an example of the heat flux map used for the bias measurement are shown in Figure 13.

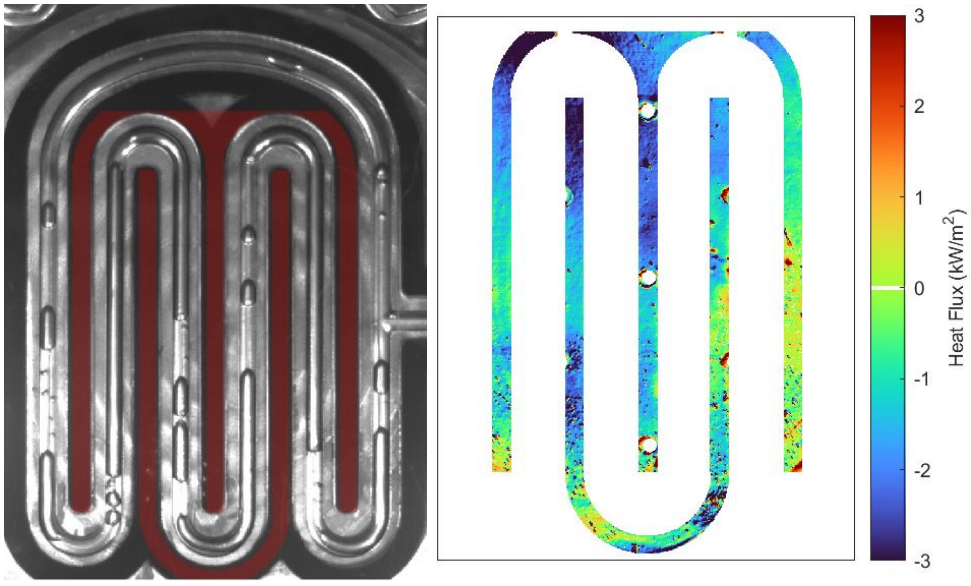

Figure 13: Areas used for bias measurement, highlighted in red at left. An example of the heat flux used for bias measurement is shown at right.

The bias values for each of the 14 videos may be seen in Figure 14 plotted against the power applied to the heater. As seen, the bias varies from -0.1 to -3.2 kW/m^2, and from -0.1 to -1.7 kW/m^2 for the subset of videos in which the heat pipe was operating. While the bias value varied between videos, it did not appear to correlate with applied heat flux. The values shown in Figure 14 were subtracted from the heat flux values for the corresponding videos. All figures showing a heat flux map within this paper have had this bias subtracted except for Figure 13.

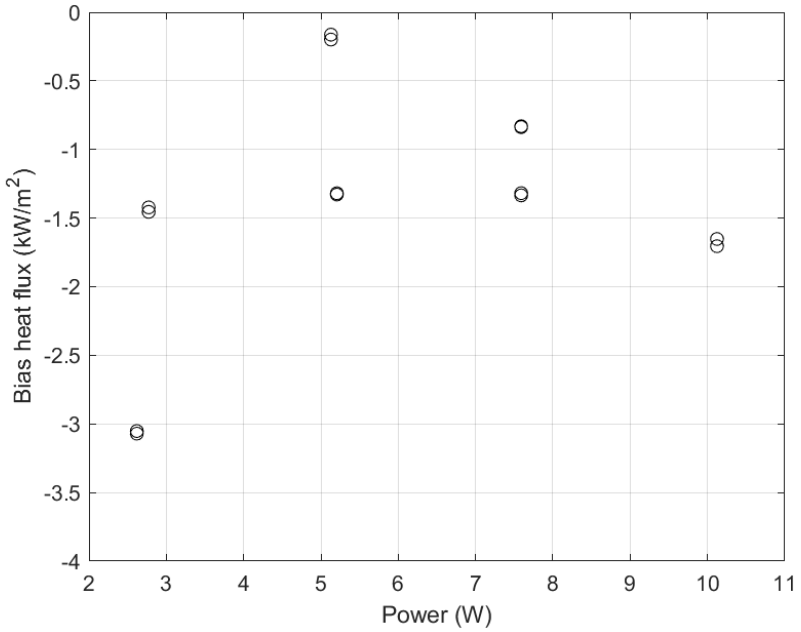

Figure 14: Bias values used for each video, plotted again power applied to heat pipe.

3.3. Additional Heat Transfer Mechanisms

In order to create a full account of the heat transfer within the heat pipe several additional sources of heat transfer were examined. In order of increasing effect, these were natural convection from the face of the heat pipe, radiation, and conduction through the sapphire. Finally, conduction through the acrylic was considered in order to validate the assumption that its contribution to the overall heat flow was negligible.

A correlation for natural convection was used in order to estimate an upper limit on the possible heat loss to natural convection [53]:

$$C_t^V = \frac{0.13\ Pr^{0.22}}{(1 + 0.61\ Pr^{0.81})^{0.42}}, \tag{8a}$$

$$\overline{C_l} = \frac{0.671}{\left[1 + \left(\frac{0.492}{Pr}\right)^{\frac{9}{16}}\right]^{\frac{4}{9}}}, \tag{8b}$$

$$Nu_l = \frac{2}{ln\left(1 + \frac{2}{\overline{C_l} Ra^{\frac{1}{4}}}\right)}, \tag{8c}$$

$$Nu_t = \frac{C_t^V Ra^{\frac{1}{3}}}{1 + 1.4 * \frac{10^9 Pr}{Ra}}, \tag{8d}$$

$$Nu = (Nu_l^6 + Nu_t^6)^{\frac{1}{6}}, \tag{8e}$$

where *Pr* represents the Prandtl number, *Ra* the Rayleigh number, C_t^V and $\overline{C_l}$ intermediate coefficients, and Nu_l, Nu_t, *and* Nu the laminar, turbulent, and overall Nusselt numbers, respectively. The heat transfer area was assumed to be that of a square with a side length of the same length as the diameter of the sapphire and the entire face was assumed to be at 70°C, the warmest temperature observed on the heater for any of the data runs. Assuming an air temperature of 25°C resulted in a total heat transfer of 0.83 W, which was much smaller than the total heat transferred.

An upper limit to the radiation heat transfer was also estimated. Assuming that the TSP was black in the IR spectrum and that the entire surface was radiating to a 25°C environment, the heat lost to radiation was calculated at 0.87 W, which was also negligible.

Conduction through the sapphire was the largest contributor to the overall heat outside of the heat transferred through the fluid. The range of possible values of the thermal conductivity, typically reported as between 25 and 50 W/m-K throughout the literature, make it difficult to provide an accurate estimate, however. Additionally, the effective width to use for heat transfer was not easy to define due to the circular shape and limited heat transfer region. The width of the heater and condenser block was used in the calculations here to provide a rough estimate. The TSP dots at two locations within the adiabatic section of the heat pipe were used to estimate the temperature of the sapphire at these locations. As these dots were roughly 14 mm apart in the vertical direction, this allowed the calculation of heat transfer through the sapphire using a simple one-dimensional conduction equation. Using a conductivity of 50 W/m-K provided conductive heat transfer ranging from 2.2 W with 2.6 W of applied power to 3.7 W with 10.1 W of applied power. Thus, while the conducted heat increased with the applied power, it did not do so linearly; the percentage of heat transferred through the sapphire steadily fell as the applied heat was increased, as shown in Figure 15.

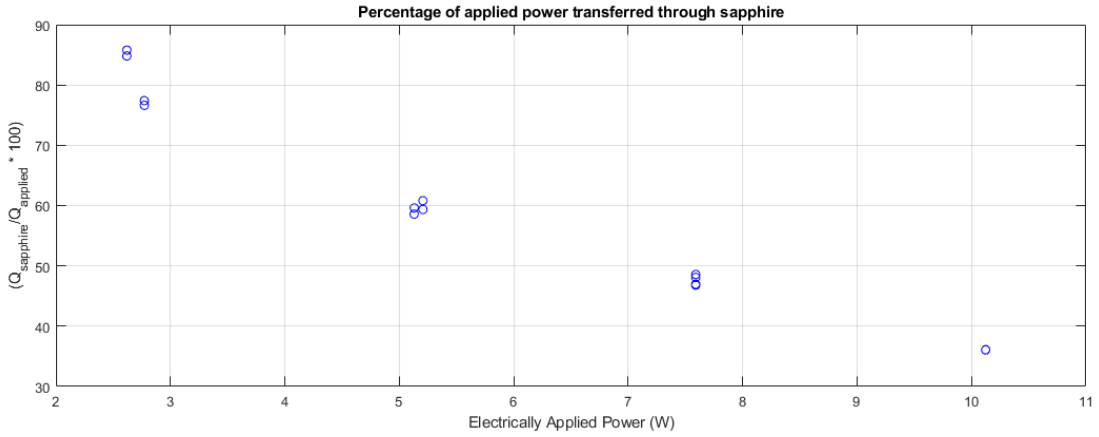

Figure 15: Percentage of applied heat transferred through the sapphire.

An upper bound on the possible conduction through the acrylic base was calculated in a similar manner to that of the sapphire. To provide an upper bound on the potential heat transfer the entire thickness of the acrylic underneath the sapphire, 16.8 mm, was used along with the width spanned by the heat pipe channels, 32.3mm, to calculate the heat transfer area. This was used with the largest temperature difference measured from the sapphire calculation along with an assumed thermal conductivity of 0.2 W/m-K for the acrylic to provide a maximum possible heat flow of 50 mW through the base. As this was two orders of magnitude less than the smallest applied power in which the heat pipe was operational, heat transfer through the acrylic was assumed to be negligible.

4. Performance and General Observations

Nucleate boiling and slight fluid motion were observed at 2.5 W of applied power. Liquid and vapor locations were largely static. Small bubbles were observed to form within the liquid in the evaporator, which would then move towards and join large static bubbles within the condenser, which would then shrink to their original size. These small bubbles and perturbations at the edges of the fluid and vapor slugs constituted the only movement observed within the heat pipe; no bulk motion was seen, even intermittently. At an applied power of 5 W, bulk fluid motion and oscillation was observed. Vapor bubbles became smaller and more interspersed within the heat pipe when compared to the concentration into two or three bubbles observed at 2.5 W. Motion was interrupted by pauses on the order of a few seconds. While these pauses retarded motion throughout the heat pipe, complete stoppage of fluid motion was only observed locally. As applied power was increased to 7.5 and then 10 W these pauses became less frequent before dying out entirely. Nucleate boiling was maintained throughout the operation. An overall circulating flow was observed

intermittently at 10 W of applied power, though was not maintained. Powers in excess of 10 W were attempted with previous iterations on the heat pipe design but resulted in burnout of the heater and so were not attempted here.

Oscillating heat pipe performance is often expressed in terms of the thermal resistance *R*, defined as

$$R = \frac{T_e - T_c}{Q}. \tag{9}$$

Here T_e refers to the temperature of the evaporator, T_c the temperature of the condenser, and Q the heat transferred by the heat pipe. For the purposes of this calculation the average temperature of the heater was used for T_e, while the temperature of the 10 mm section immediately below the condenser block was taken as T_c. The resulting resistance values for each data run are shown in Figure 16. It should be noted that these values use the power applied to the heater, and so include the additional heat transfer mechanisms noted in the previous section. As is typical for OHPs, thermal resistance was seen to fall with increasing power from a maximum value of roughly 2.3 K/W to a minimum of 1 K/W.

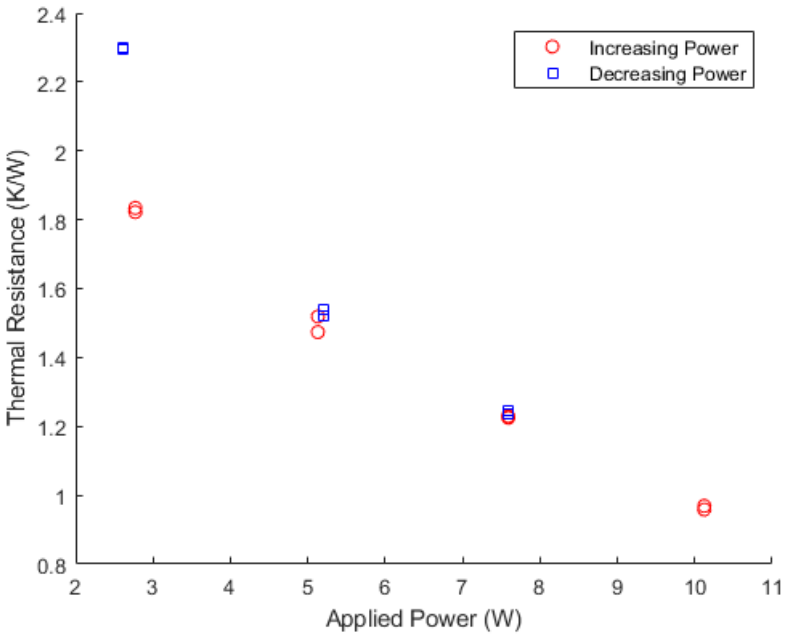

Figure 16: Heat pipe thermal resistance variation with applied power.

An example of the converted heat pipe temperature and calculated heat flux is shown in Figure 17 alongside the corresponding visual recording. The top of this image corresponds to the evaporator section, while the bottom comprises the heater. Positive heat flux values indicate heat flow from the sapphire into the working fluid.

Wall heat flux was highest when vapor bubbles passed over the surface in both the evaporator and condenser, and was typically around 5 W/m^2 greater in magnitude when vapor was present. Furthermore, the wall temperature when vapor bubbles were present was nearly uniform. Standard deviation in the wall temperature under vapor bubbles, even those spanning the entire heat pipe, was typically under 2°C. This compares to the 15 to 25°C temperature difference between the heater and condenser regions. Vapor bubbles that dwelled in the evaporator were often seen to develop the heat flux pattern shown in Figure 17, in which heat transfer remained high near the edges of the bubble but fell to near zero at its center. This was interpreted as indicating the presence of a liquid film around the

bubble that had achieved dry-out at its location closest to the heater. Combined, these observations led to the conclusion that the vapor bubbles were surrounded by a liquid film at saturation conditions. This conclusion is examined in more detail in the following sections.

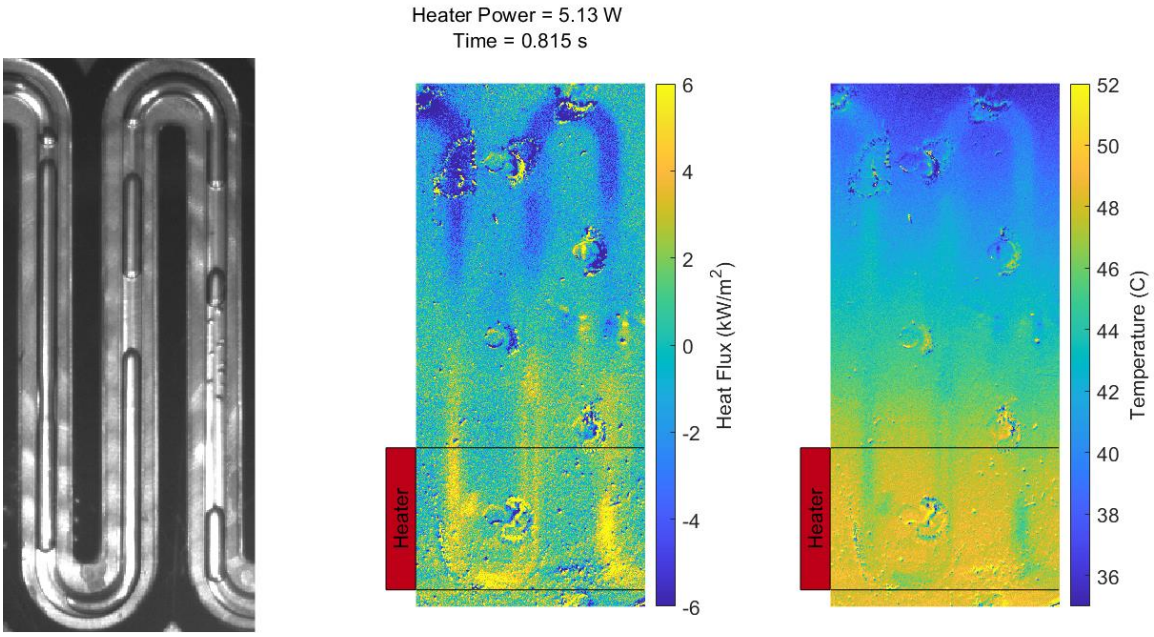

Figure 17: Comparison of visual data (left), temperature data (right), and calculated heat flux (center). Heat transfer is reaches its largest magnitude along the vapor bubbles. Note the dryout of the bubble in the center channel shown here.

5. Analysis of Heat Transfer Mechanism

The dominant heat transfer mechanism within the heat pipe is examined in detail below. It was assumed that the liquid film surrounding the vapor bubbles was at saturation conditions, so that the dominant mechanism of heat transfer around the vapor slugs was evaporation or condensation from or to this liquid film. This led to the further assumption that heat transfer over vapor bubbles as due primarily to latent heat transfer, while heat

transfer within the liquid slugs was due to sensible heating. As this assumption was critical to the analysis following a verification of it was performed using two methods.

5.1. Latent Heat Transfer Verification

It must be verified that the heat transfer overtop of the bubbles was not due to convection, i.e., that heat was not transferred by subcooling the liquid film in the condenser and warming it in the evaporator. Important to this analysis was an estimate of the film thickness around the vapor bubbles, as this allowed the calculation of both an overall heat capacity and a time constant for the liquid film. Han and Shikazono performed a thorough analysis of liquid film thickness around vapor bubbles during slug flow for channel dimensions, flow conditions, and working fluids similar to the ones used here [54]. As such, their experimental correlation was used here to estimate the liquid film thickness:

$$\frac{\delta_0}{D} = \frac{0.670Ca^{\frac{2}{3}}}{1 + 3.13Ca^{\frac{2}{3}} + 0.504Ca^{0.672}Re^{0.589} - 0.352We^{0.629}}. \quad (10)$$

Here δ_0 represents the liquid film thickness, D the diameter of the channel, here taken to be the hydraulic diameter, *Ca* the capillary number, *Re* the Reynold's number, and *We* the Weber number. This correlation uses the liquid properties for the density, viscosity, and heat capacity terms. The equation further assumes a Reynold's number less than 2000. While liquid velocity was held constant for the derivation of equation (10) it varied continuously during operation of the heat pipe. In order to provide a conservative estimate the highest observed liquid velocity within the heat pipe was used for calculation as this results in the largest film thickness as calculated using equation (10). This velocity of 210 mm/s resulted in a calculated Reynold's number of 1140 and a film thickness of 35 μm. This film thickness could then be used to calculate a thermal time constant for the liquid

film using equation (4), where τ_0 represents the liquid film thermal time constant and α the thermal diffusivity of the liquid HFE-7000. For a film thickness of 35 μm this time constant was calculated as 28 ms. As will be discussed in in the next section, a transition period of 2-4 times this time was seen in the heat flux data when a liquid slug was replaced by a vapor bubble. Further, this time period is considerably shorter than the hundreds of milliseconds to seconds in which a given vapor bubble typically covered one point on the heat pipe. This analysis indicated the liquid film rapidly reached the saturation temperature, and that heat transferred due to sensible heating and cooling of the liquid film could be neglected.

A second verification was performed using the visual data. The mass of a bubble within the condenser could be estimated at each time stamp as it shrank based upon its size as seen in the visual footage. This mass loss could then be used to estimate the latent heat transfer required to affect this shrinkage, and this latent estimate compared to the TSP measured heat transfer overtop the bubble. A close match between this visual estimate and the TSP data would then serve to confirm latent heat transfer as being the main method by which heat was transferred overtop bubbles.

The 35 μm maximum film thickness estimated above is small compared to the 1.6 mm channel width. The cross-sectional area of vapor within a bubble was therefore estimated as the cross sectional area of the entire channel. The mass of the vapor in the slug was then be taken to be

$$m_v = \rho_v A_c L_s, \tag{11}$$

where m_v is the mass of the vapor in the slug, ρ_v the density of the vapor, and L_s the length of the slug. The density was taken to be the density of vapor at saturation at the average TSP measured temperature over the face of the bubble. L_s was measured by taking the number of pixels between the top and bottom of the slug, then converting from pixel length to actual length by comparing the pixel distance of two points on the image with a known actual distance. For each selected bubble this mass was calculated at each frame to provide a time history. This was then be converted into an estimated latent heat transfer using the equation

$$Q_{latent} = h_{fg} \frac{dm_v}{dt}, \tag{12}$$

where Q_{latent} indicates the visually estimated latent heat transfer and h_{fg} the latent heat of vaporization. As with the vapor density, this latter parameter was taken to be the saturation value at the TSP measured average temperature of the slug.

The most straightforward way to estimate the dm_v/dt term in equation (12) would have been to perform a finite difference calculation on the calculated mass. However, the manually determined endpoints of the vapor bubbles had some inherent error, functionally similar to noise in the data. This was small when taken over the entire timescale, but significant when comparing immediately adjacent points, as is done with a finite difference estimation. To avoid this error the change in mass with time was instead estimated by fitting a fifth order polynomial to the calculated mass. The derivative of this polynomial was then used to estimate dm_v/dt. An example of the calculated mass with time and its corresponding polynomial fit is shown in Figure 18. This estimated latent heat transfer was then compared with the heat transfer estimated from the TSP measurements. Two such comparisons are shown in Figure 19.

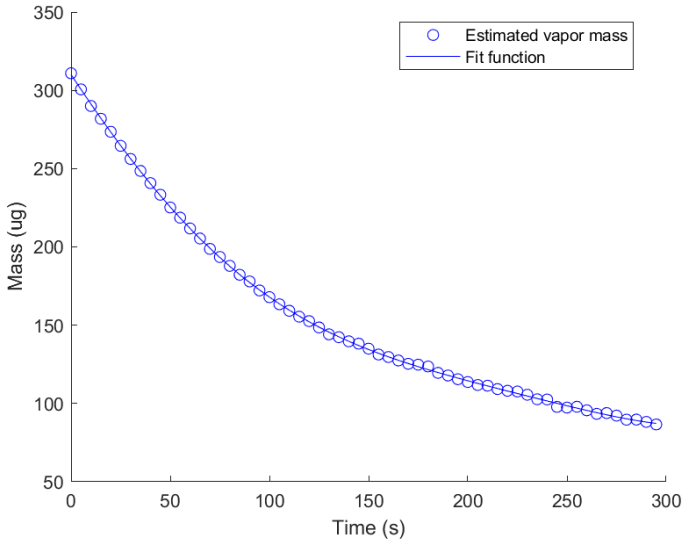

Figure 18: Calculated mass loss alongside polynomial fit used to determine its derivative. The values shown here correspond to the 5.13 W case shown in Figure 19.

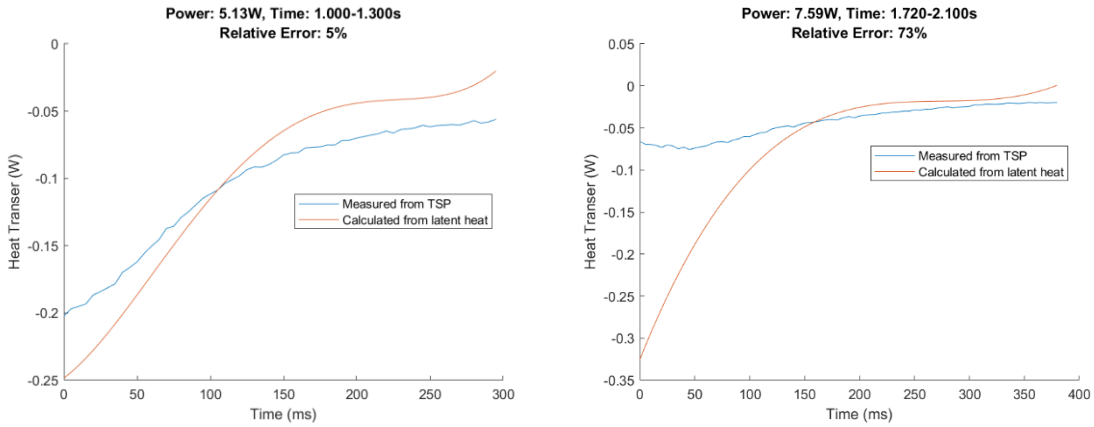

Figure 19: TSP and visually estimated heat transfer for two vapor slugs within the heat pipe condenser.

To determine an overall error the two power estimates were integrated over time to provide a total energy transfer. The difference in energy between the two estimations was then divided by the TSP measured energy to provide a relative error. Ten bubbles were examined, one from each video in which the heat pipe was operating. The resulting errors are plotted against applied power in Figure 20. In seven out of the ten cases examined the

relative error was less than 45%, with half of the cases showing an error of less than 20%. Of the remaining three cases two had errors between 65% and 75%, with the largest error at 121%. As the median and mean errors were 23.5% and 39%, respectively, these larger errors were treated as outliers. This 39% average error was taken to indicate confirmation of the validity latent heat transfer assumption. This assumption, corroborated by both this and the liquid film time constant analysis above, was therefore used for all subsequent analysis.

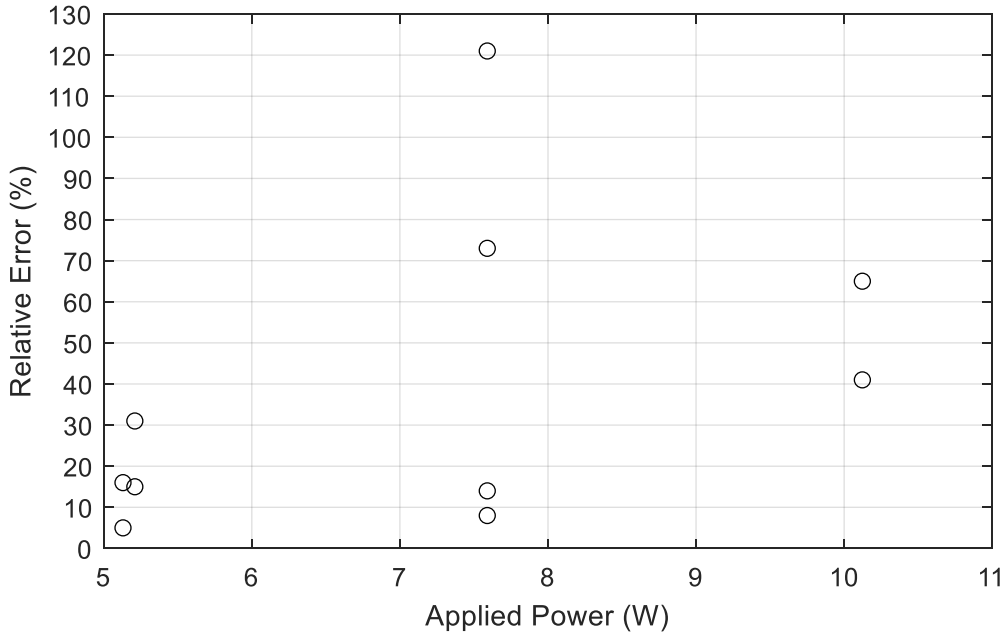

Figure 20: Estimated relative error in latent heat transfer assumption.

5.2. Latent vs Sensible Selection

As detailed above, it was assumed that wall heat transfer when vapor bubbles were present was due to latent heat transfer, while heat transfer overtop the liquid slugs was due to sensible heat transfer. It was further assumed that heat transfer with the acrylic (the heat pipe substrate) was negligible, as was conductive heat transfer between the vapor bubble

and adjacent liquid slugs. With these assumptions, the relative latent and sensible contributions to the overall heat transfer could be estimated by comparing the heat transfer at a point when it was covered by vapor or liquid, respectively. For each of the 10 videos in which the heat pipe was operating (input powers from 5 to 10 W) 10 points were examined. These points were positioned at constant intervals vertically going from the center of the top loop of the selected channel to the center of its bottom loop, as is shown in Figure 21. Intermediate points were placed in the center of the heat pipe channel horizontally. At each point the mode of heat transfer, latent or sensible, was selected for each of the 1000 frames in the video was based upon whether the location was covered by vapor or liquid.

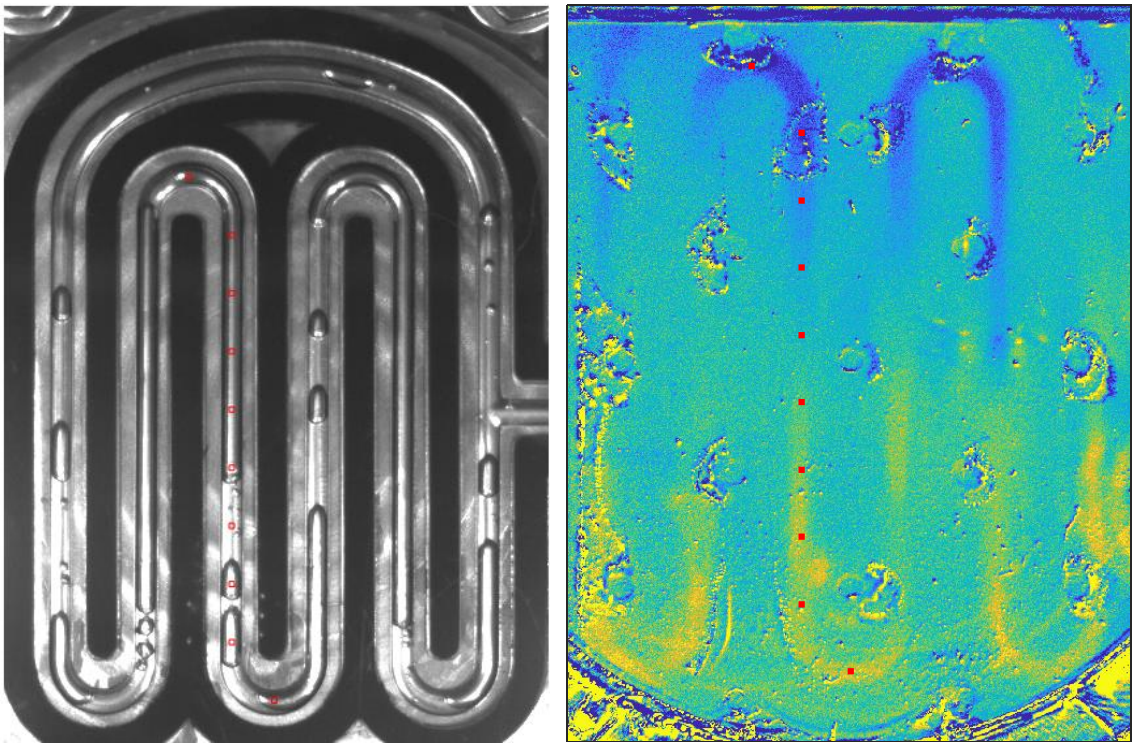

Figure 21: Points used for sensible/latent heat transfer comparison. Visual data shown at left, with heat flux data at right.

This selection was performed using a Matlab script examining the pixel intensity at the given point. It was found that the mean pixel intensity for liquid coverage was roughly 40 points higher than that for vapor, allowing the program to select the phase type by whether the intensity was above or below the overall data mean. When compared with manually chosen values this automated selection was found to produce the correct result for greater than 85% of all points. Examination of the improperly selected points revealed that they all occurred at transitions between the two phases or at values far from the mean liquid and vapor intensities. Moreover, the incorrect points were all identified as liquid. That is, in no case did the program incorrectly mark a point as being covered by vapor when it was covered by liquid; all mistakes were instances in which vapor coverage was identified as liquid coverage. To correct these selections the program was set to flag points that were identified as liquid and either more than one standard deviation from the mean liquid value or which were preceded or followed by a change in intensity of more than a set threshold. These flagged points were then presented to the user of the program for verification or correction. Typically, between 250 and 300 frames of each 1000 frame video were flagged in this manner. When compared against a video in which the points had been manually selected only two points were selected incorrectly and not flagged. A 0.2% error in selection was deemed acceptable, and this selection program was therefore run on the remainder of the data. An example showing the intensity over time at a point with the corresponding selections may be seen in Figure 22 with the flagged locations circled in red.

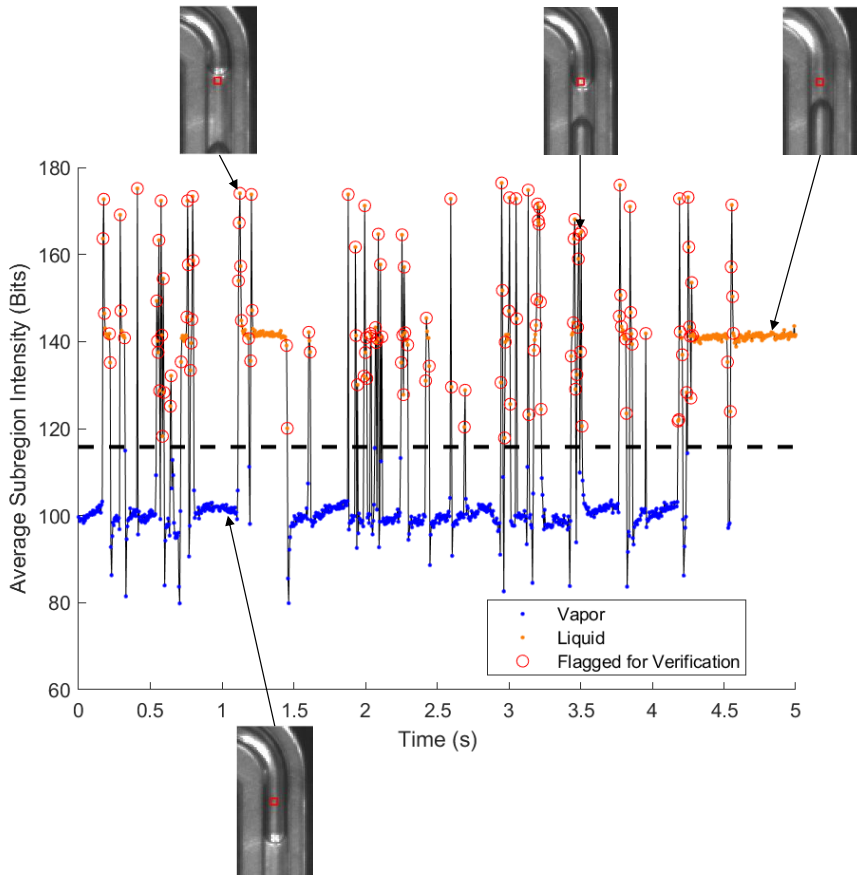

Figure 22: Example phase selection showing points flagged for verification. The data mean, used to distinguish the phases, is shown by a dashed line.

5.3. Results

Two examples of the selected heat transfer types and the corresponding heat flux values are shown in Figure 23. In this figure traces are shown for the top and bottom-most points shown in Figure 21. As may be seen, heat transfer was consistently higher in magnitude when the point was covered by vapor, and transitions from a liquid slug to a vapor bubble corresponded to a rapid increase in heat flux in all cases. This is consistent with a heat transfer dominated by condensation through or evaporation of the liquid film surrounding each bubble. Moreover, the time required for this transition was typically between 40 and 140 ms, which agrees well with the calculated liquid film time constant derived above.

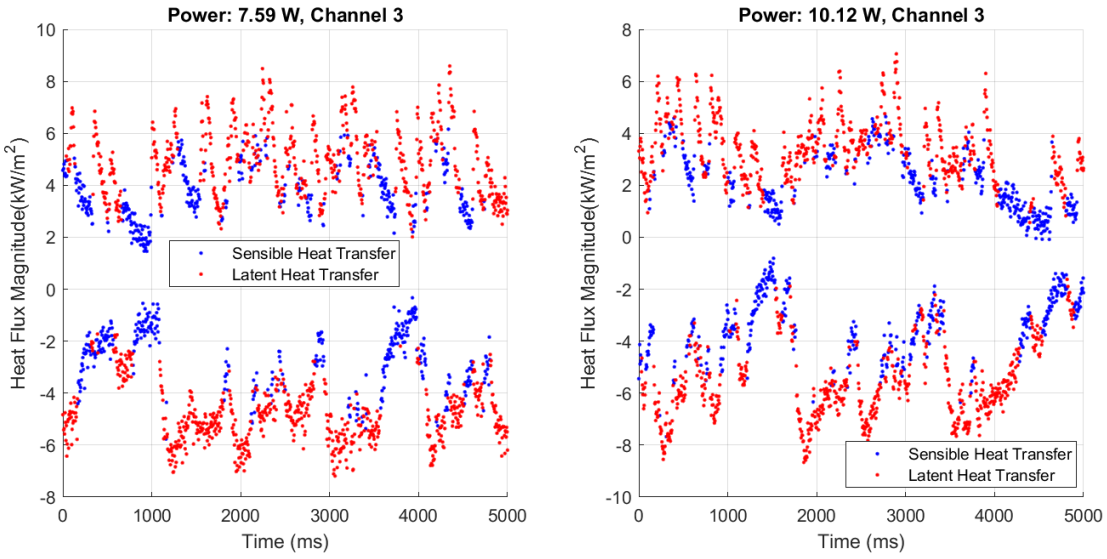

Figure 23: Sensible and latent contributions to the overall heat flux for two different videos. Two traces are shown – the top (positive) from the evaporator and the bottom from the condenser.

The analysis above further allowed the calculation of the relative contribution of sensible and latent heat transfer to the overall heat flux. To do this the sum of the heat flux values in which the channel was covered by a vapor bubble was divided by the sum of all 1000 heat flux values at that location to provide the latent percentage, and likewise with liquid coverage for sensible heating and cooling. This summation was performed on the absolute value of the heat flux in order to prevent data points from canceling one another within the regions near the center of the heat pipe where heat transfer was not universally in one direction. An example of this analysis may be seen in Figure 24. As shown, the latent contribution was consistently between 70% and 90% at all locations within the heat pipe. Performing this heat transfer analysis for all operational videos, as is done in Figure 25, revealed a latent contribution of between 68% and 85% for all data runs, with a mean

contribution of 78%. This result is consistent with the 66 to 74% latent contribution reported by Jo et al. [42].

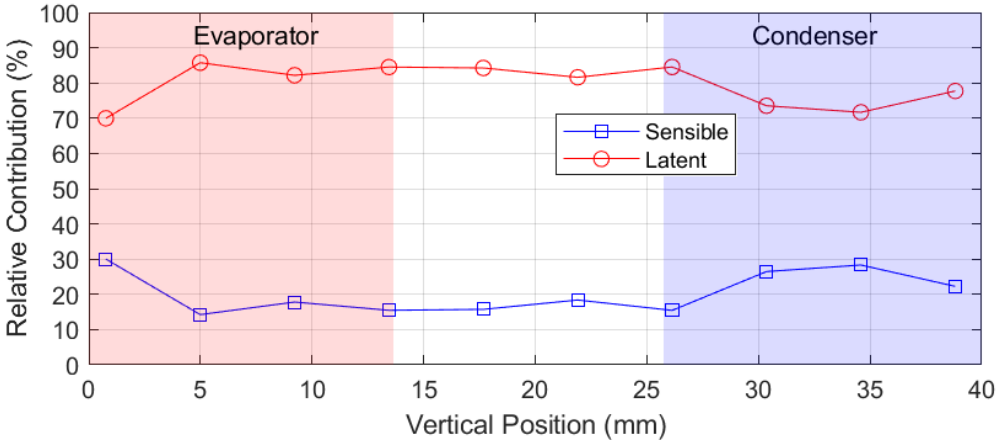

Figure 24: Relative contribution of sensible and latent heat transfer to overall heat transfer. Positions listed relative to the lowermost edge of heat pipe channels.

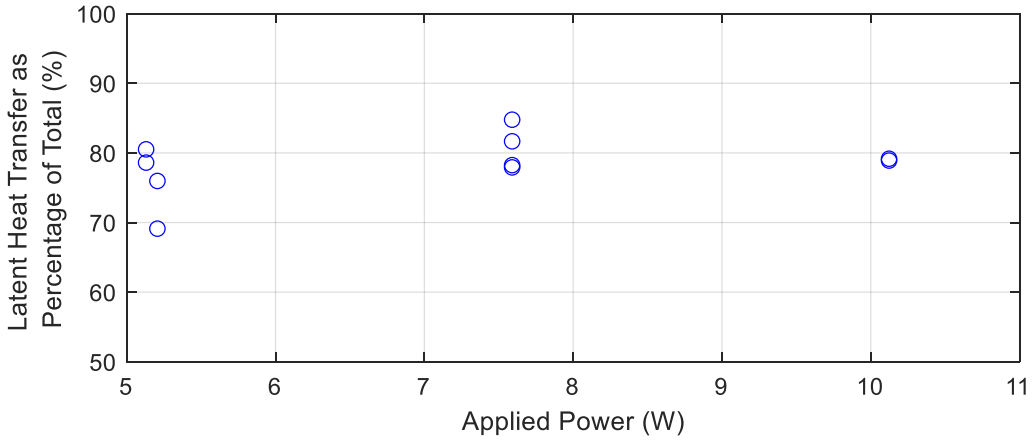

Figure 25: Latent heat transfer contribution for all data sets in which the heat pipe was operational.

It was additionally possible to perform an instantaneous calculation of the relative contributions of latent and sensible heat by dividing an individual frame into latent and sensible sections and calculating the contributions of each to the total heat transfer. While the greater user involvement required to select regions prohibited this method from being

used at each of the 1000 frames for each video, its use on selected frames provided a confirmation of the results detailed above, specifically that the selection of points was not contributing to a bias in the results. For each video in which the heat pipe was operating 10 frames, equally spaced in time, were chosen for this analysis. For each frame thus selected the heat pipe was manually sectioned into sections of liquid and vapor, an example of which is shown in Figure 26. Here red regions indicate liquid (sensible heat transfer), while blue indicates vapor (latent heat transfer). The left and right-most channels were excluded from the analysis due to significant damage to the TSP overtop these channels.

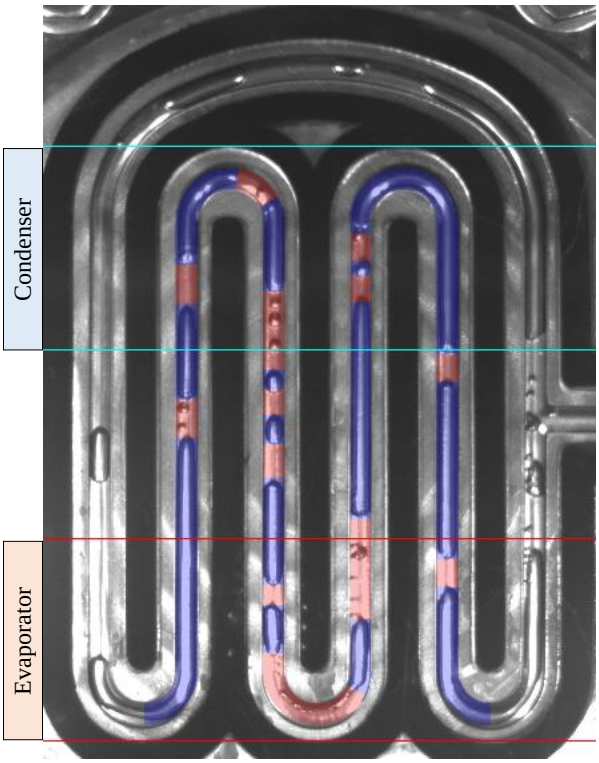

Figure 26: Identified locations of vapor and liquid slugs within the heat pipe. Red is used to indicate liquid while blue indicates vapor.

When compared with the point examination the analysis performed in this manner attributed a lower, though still dominant, percentage of the heat transfer to latent heating and cooling. Of the 10 videos analyzed, the minimum latent contribution was 65%, the

maximum 78%, and the average 72%. Latent heating within the evaporator was in-line with, though slightly below, these values, with minimum, maximum, and mean latent contributions of 62%, 78%, and 70%, respectively. The contribution within the condenser was higher, with respective values of 68%, 83%, and 72%. These results may be seen summarized in Figure 27.

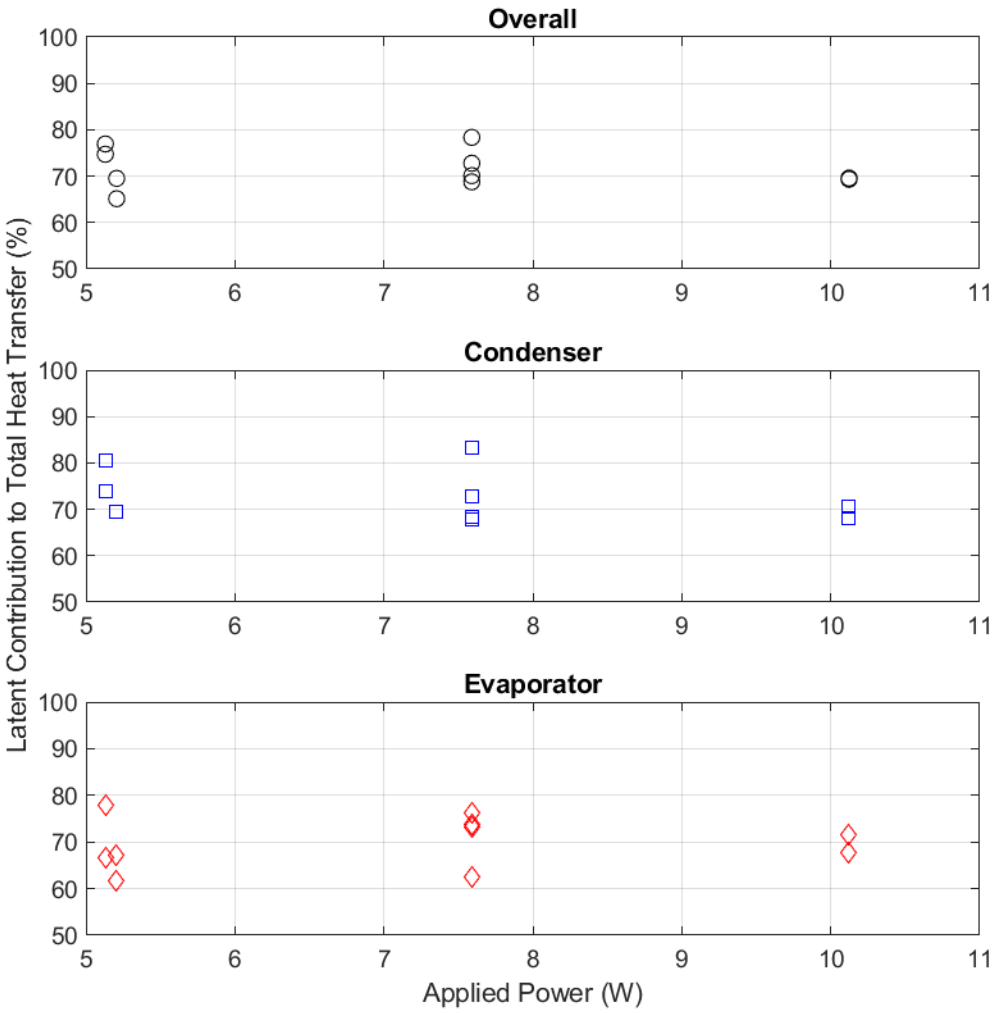

Figure 27: Summary of calculated latent contribution.

6. Conclusion and Future Work

6.1. Conclusion

A visual measurement technique utilizing temperature sensitive paints was used in order to measure temperature and heat transfer across the face of an oscillating heat pipe. This was done by recording the response of a layup using temperature sensitive paint placed on one side of the heat pipe. Visual data of the heat pipe flow mechanics were recorded using a second camera placed on the other side of the heat pipe. The mechanism and experimental setup are described in detail in chapter 2. Analysis of the acquired data, described in detail in chapter 3, indicated a thermal resistance of 1 K/W to 2.3 K/W for this design. Further, in chapter 4 heat flux was shown to concentrate around the vapor bubbles both within the evaporator and condenser. In chapter 5 it was shown that the heat transfer when vapor bubbles were present as dominated by latent heat transfer, and that the contribution of latent heat transfer to the overall OHP heat transfer was between 65% and 85% for the design considered here.

6.2. Suggested Changes to Design and Future Work

Initial work should focus on improving the quality of the measurement taken. While the work performed here proves the viability of this method, the apparatus used has several shortcomings. First, the sapphire used as the front plate for the TSP layer provided a conductive path with thermal resistance on the same order as the heat pipe itself. A better measurement could be taken by breaking this additional thermal path, either by using a thinner piece of sapphire or creating the adiabatic section out of a different material with a lower thermal conductivity. This latter option would also provide a more distinct adiabatic

section within the heat pipe. Alternately, the performance of the heat pipe could be improved enough to make the sapphire conduction contribution small in comparison.

Additionally, the dots of TSP used for the sapphire temperature produced depressions within the acrylic adhesive layer. These led to trapped air bubbles underneath the dots, which were spread when force was applied to the sapphire to seal the gasket and damaged the TSP around the dots. This could be solved either by better controlling the thickness of the TSP used for these dots, or by utilizing an adhesive less sensitive to the increased thickness. A transparent epoxy would likely work quite well and would additionally be less likely to deform around the gaskets.

Third, the uncertainty in the heat flux measurement was of the same order as the data itself, and so efforts should be taken to reduce this in future measurements. Increasing the performance of the heat pipe, and so the measured heat flux values, would be one viable approach. Reducing uncertainty would likely require reducing the camera noise, as this was the primary contributor to the error in the heat flux. Increasing exposure time to reduce noise would reduce the quality of the measurement, and the Photometrics Prime camera used for the TSP measurement has a very low inherent noise. As such, noise reduction through spatial binning would be the most promising approach.

The heat flux data from this work showed a consistent negative bias. The cause was not discovered here, but future experiments should take steps to remove this error. Bleaching of the TSP or warmup transients in the UV LEDs, turned on just prior to measurement to reduce the risk of bleaching, could be contributors. A shutter placed in front of the TSP would allow shorter, more controlled exposure to UV light while also allowing the UV LEDs to be left on, so would likely produce more consistent results.

Finally, the design used here had the horizontal connecting channel of the heat pipe covered by the condenser. As a result, data could not be taken over this section. This was done to improve the performance of the heat pipe, but future experiments should attempt to move the condenser block fully off the heat pipe or remove heat in another manner.

With these improvements made and problems fixed, the measurement technique used here is well suited to a parametric heat pipe study. The gasket design used here would allow the TSP stackup to be quickly changed between designs, and the use of acrylic as the base material allows inexpensive construction of new designs.

7. References

[1] T. Mito *et al.*, "Achievement of high heat removal characteristics of superconducting magnets with imbedded oscillating heat pipes," *IEEE Trans. Appl. Supercond.*, vol. 21, no. 3 PART 2, pp. 2470–2473, 2011.

[2] D. Mangini, M. Mameli, A. Georgoulas, L. Araneo, S. Filippeschi, and M. Marengo, "A pulsating heat pipe for space applications: Ground and microgravity experiments," *Int. J. Therm. Sci.*, vol. 95, pp. 53–63, 2015.

[3] S. M. Thompson, P. Cheng, and H. B. Ma, "An experimental investigation of a three-dimensional flat-plate oscillating heat pipe with staggered microchannels," *Int. J. Heat Mass Transf.*, vol. 54, no. 17–18, pp. 3951–3959, 2011.

[4] K. Natsume *et al.*, "Development of cryogenic oscillating heat pipe as a new device for indirect/conduction cooled superconducting magnets," *IEEE Trans. Appl. Supercond.*, vol. 22, no. 3, p. 4703904, 2012.

[5] J. Gu, M. Kawaji, and R. Futamata, "Effects of Gravity on the Performance of Pulsating Heat Pipes," *J. Thermophys. HEAT Transf.*, vol. 18, no. 3.

[6] G. H. Kwon and S. J. Kim, "Experimental investigation on the thermal performance of a micro pulsating heat pipe with a dual-diameter channel," *Int. J. Heat Mass Transf.*, vol. 89, pp. 817–828, 2015.

[7] S. Jun and S. J. Kim, "Comparison of the thermal performances and flow characteristics between closed-loop and closed-end micro pulsating heat pipes," *Int. J. Heat Mass Transf.*, vol. 95, pp. 890–901, 2016.

[8] A. Yoon and S. J. Kim, "Characteristics of oscillating flow in a micro pulsating heat pipe: Fundamental-mode oscillation," *Int. J. Heat Mass Transf.*, vol. 109, pp. 242–

253, 2017.

[9] Y. J. Youn and S. J. Kim, “Fabrication and evaluation of a slicon-based micro pulsating heat spreader,” *Sensors Actuators, A Phys.*, vol. 174, no. 1, pp. 189–197, 2012.

[10] A. Yoon and S. J. Kim, “Understanding of the thermo-hydrodynamic coupling in a micro pulsating heat pipe,” *Int. J. Heat Mass Transf.*, vol. 127, pp. 1004–1013, Dec. 2018.

[11] J. Lee and S. J. Kim, “Effect of channel geometry on the operating limit of micro pulsating heat pipes,” *Int. J. Heat Mass Transf.*, vol. 107, pp. 204–212, 2017.

[12] H. Akachi, “Structure of a Heat Pipe,” 1990.

[13] P. Charoensawan, S. Khandekar, M. Groll, and P. Terdtoon, “Closed loop pulsating heat pipes - Part A: Parametric experimental investigations,” *Appl. Therm. Eng.*, vol. 23, no. 16, pp. 2009–2020, 2003.

[14] X. M. Zhang, J. L. Xu, and Z. Q. Zhou, “Experimental study of a pulsating heat pipe using fc-72, ethanol, and water as working fluids,” *Exp. Heat Transf.*, vol. 17, no. 1, pp. 47–67, 2004.

[15] N. Kammuang-Lue, P. Sakulchangsatjatai, P. Terdtoon, D. J. Mook, & D. J. Mook, and D. J. Mook, “Correlation to Predict the Maximum Heat Flux of a Vertical Closed-Loop Pulsating Heat Pipe,” *Heat Transf. Eng.*, vol. 30, no. 12, pp. 961–972, Oct. 2010.

[16] S. Khandekar, A. P. Gautam, and P. K. Sharma, “Multiple quasi-steady states in a closed loop pulsating heat pipe,” *Int. J. Therm. Sci.*, vol. 48, no. 3, pp. 535–546, 2009.

[17] Y. Zhang and A. Faghri, “Advances and Unsolved Issues in Pulsating Heat Pipes,” *Heat Transf. Eng.*, vol. 29, no. 1, pp. 20–44, 2008.

[18] B. S. Taft, A. D. Williams, and B. L. Drolen, “Review of Pulsating Heat Pipe Working Fluid Selection,” *J. Thermophys. Heat Transf.*, vol. 26, no. 4, pp. 651–656, 2012.

[19] J. Qu, H. Wu, and P. Cheng, “Start-up, heat transfer and flow characteristics of silicon-based micro pulsating heat pipes,” *Int. J. Heat Mass Transf.*, vol. 55, no. 21–22, pp. 6109–6120, 2012.

[20] H. Ma, *Oscillating Heat Pipes*. New York: Springer, 2015.

[21] H. Han, X. Cui, Y. Zhu, and S. Sun, “A comparative study of the behavior of working fluids and their properties on the performance of pulsating heat pipes (PHP),” *Int. J. Therm. Sci.*, vol. 82, pp. 138–147, 2014.

[22] S. Khandekar, M. Schneider, R. Schafer, R. Kulenovic, and M. Groll, “Thermofluid Dynamic Study of Flat-Plate Closed-Loop Pulsating Heat Pipes,” *Microscale Thermophys. Eng.*, vol. 6, pp. 303–317, 2002.

[23] H. Yang, S. Khandekar, and M. Groll, “Performance characteristics of pulsating heat pipes as integral thermal spreaders,” *Int. J. Therm. Sci.*, vol. 48, pp. 815–824, 2009.

[24] W. Jiansheng, W. Zhenchuan, and L. Meijun, “Thermal performance of pulsating heat pipes with different heating patterns,” *Appl. Therm. Eng.*, vol. 64, no. 1–2, pp. 201–212, 2014.

[25] H. Yang, S. Khandekar, and M. Groll, “Operational limit of closed loop pulsating heat pipes,” *Appl. Therm. Eng.*, vol. 28, no. 1, pp. 49–59, 2008.

[26] S. M. Thompson and H. B. Ma, “A STATISTICAL ANALYSIS OF

TEMPERATURE OSCILLATIONS ON A FLAT-PLATE OSCILLATING HEAT PIPE WITH TESLA-TYPE CHECK VALVES," vol. 2, p. 33002, 2011.

[27] W. Kim and S. J. Kim, "Effect of reentrant cavities on the thermal performance of a pulsating heat pipe," *Appl. Therm. Eng.*, vol. 133, pp. 61–69, 2018.

[28] J. Qu, X. Li, Q. Xu, and Q. Wang, "Thermal performance comparison of oscillating heat pipes with and without helical micro-grooves," *Heat Mass Transf.*, vol. 53, no. 11, pp. 3383–3390, 2017.

[29] H. B. Ma, A. M. A. Hanlon, and A. C. L. Chen, "An investigation of oscillating motions in a miniature pulsating heat pipe," *Microfluid. Nanofluidics*, vol. 2, no. 2, pp. 171–179, 2006.

[30] J. Qu and H. Wu, "Thermal performance comparison of oscillating heat pipes with SiO 2 /water and Al 2 O 3 /water nanofluids," *Int. J. Therm. Sci.*, vol. 50, no. 10, pp. 1954–1962, 2011.

[31] R. R. Riehl and N. dos Santos, "Water-copper nanofluid application in an open loop pulsating heat pipe," *Appl. Therm. Eng.*, vol. 42, pp. 6–10, 2012.

[32] H. B. Ma *et al.*, "Effect of nanofluid on the heat transport capability in an oscillating heat pipe," *Appl. Phys. Lett.*, vol. 88, no. 14, 2006.

[33] V. K. Karthikeyan, S. Khandekar, B. C. Pillai, and P. K. Sharma, "Infrared thermography of a pulsating heat pipe: Flow regimes and multiple steady states," *Appl. Therm. Eng.*, vol. 62, no. 2, pp. 470–480, 2014.

[34] W. Qu and H. B. Ma, "Theoretical analysis of startup of a pulsating heat pipe," *Int. J. Heat Mass Transf.*, vol. 50, no. 11–12, pp. 2309–2316, 2007.

[35] H. B. Ma, B. Borgmeyer, P. Cheng, and Y. Zhang, "Heat Transport Capability in an

Oscillating Heat Pipe," *J. Heat Transfer,* vol. 130, no. 8, p. 081501, 2008.

[36] Y. Zhang and A. Faghri, "Heat transfer in a pulsating heat pipe with open end," *Int. J. Heat Mass Transf.*, vol. 45, no. 4, pp. 755–764, Feb. 2002.

[37] W. Shao and Y. Zhang, "Effects of Film Evaporation and Condensation on Oscillatory Flow and Heat Transfer in an Oscillating Heat Pipe," *J. Heat Transfer,* vol. 133, no. 4, p. 042901, 2011.

[38] M. B. Shafii, A. Faghri, Y. Zhang, and M. Asme, "Thermal Modeling of Unlooped and Looped Pulsating Heat Pipes," *J. Heat Transfer,* vol. 123, pp. 1159–1172, 2001.

[39] S. Khandekar and M. Groll, "An insight into thermo-hydrodynamic coupling in closed loop pulsating heat pipes," *Int. J. Therm. Sci.*, vol. 43, no. 1, pp. 13–20, 2004.

[40] B. Mehta and S. Khandekar, "Taylor bubble-train flows and heat transfer in the context of Pulsating Heat Pipes," *Int. J. Heat Mass Transf.*, vol. 79, pp. 279–290, 2014.

[41] V. S. Nikolayev, "A Dynamic Film Model of the Pulsating Heat Pipe," *J. Heat Transfer,* vol. 133, no. 8, p. 081504, 2011.

[42] J. Jo, J. Kim, and S. J. Kim, "Experimental investigations of heat transfer mechanisms of a pulsating heat pipe," *Energy Conserv. Manag.*, vol. 181, pp. 331–341, 2019.

[43] H. Al Hashimi, C. F. Hammer, M. T. Lebon, D. Zhang, and J. Kim, "Phase-Change Heat Transfer Measurements Using Temperature-Sensitive Paints," *J. Heat Transfer,* vol. 140, no. 3, p. 031601, 2017.

[44] M. T. Lebon, C. F. Hammer, and J. Kim, "Gravity effects on subcooled flow boiling heat transfer," *Int. J. Heat Mass Transf.*, vol. 128, pp. 700–714, 2019.

[45] 3M Novec, “3M Novec 7000 Engineered Fluid.” 2009.

[46] 3M Novec, “3M Novec 7100 Engineered Fluid,” *Design-basis Accident Analysis Methods For Light-water Nuclear Power Plants*. 2009.

[47] NIST, “Water,” *NIST Chemistry WebBook*, 2018. [Online]. Available: https://webbook.nist.gov/cgi/cbook.cgi?ID=C64175&Mask=4#Thermo-Phase.

[48] NIST, “Ethanol,” *NIST Chemistry WebBook*, 2018. [Online]. Available: https://webbook.nist.gov/cgi/cbook.cgi?ID=C64175&Mask=4#Thermo-Phase.

[49] NIST, “Acetone,” *NIST Chemistry WebBook*, 2018. [Online]. Available: https://webbook.nist.gov/cgi/cbook.cgi?ID=C67641&Mask=4#Thermo-Phase.

[50] M. H. Rausch, L. Kretschmer, S. Will, A. Leipertz, and A. P. Fröba, “Density, surface tension, and kinematic viscosity of hydrofluoroethers HFE-7000, HFE-7100, HFE-7200, HFE-7300, and HFE-7500,” *J. Chem. Eng. Data*, vol. 60, no. 12, pp. 3759–3765, 2015.

[51] 3M, “3M Thermal Management Fluids: Cool Under Fire - Dielectric heat transfer fluid solutions for military and aerospace applications.” 2009.

[52] G. P. Peterson, *An Introduction to Heat Pipes Modeling, Testing, and Applications*. New York: John Wiley & Sons, Inc., 1994.

[53] G. D. Raithby and K. G. . Hollands, “Chapter 4. Natural Convection,” in *Handbook of Heat Transfer*, 3rd ed., W. M. Rohsenow, J. P. Hartnett, and Y. I. Cho, Eds. New York: McGraw-Hill, 1998, pp. 4.1-4.99.

[54] Y. Han and N. Shikazono, “Measurement of the liquid film thickness in micro tube slug flow,” *Int. J. Heat Fluid Flow*, vol. 30, pp. 842–853, 2009.